qualitative data, and a quantitative analysis of the VEGFR distribution required to regulate the behavior of these cells has not been carried out in vivo. In addition, previous ex vivo data revealed that the amount of VEGFR protein involved in angiogenesis in ischemic tissue is 13-fold greater than in normal tissues.[15] In this report, however, because the total amount of VEGFR in both the vessel wall and the extravascular area was measured, the detailed quantitative distribution of VEGFR was not known. Our results suggest that only an approximately 3-fold difference in VEGFR distribution on the vascular wall is involved in the formation of branched vasculature from linear vasculature during angiogenesis (Figure 6I). The increase in VEGFR levels we observe after ischemia may quantitatively reveal a gradient of VEGFR expression levels between the stalk cells and pharynx cells.

Our results indicate that VEGFR distribution in in vivo ischemic tissues increased gradually over a specific period and remained steady at an approximately 3-fold increase. To increase the number of sprouting vessels for the operation of ischemic hypoxia, the steady several-fold increase of VEGFR expression levels at the ischemic site may be effective for controlled angiogenesis. Previously, treatment against ischemic hypoxia using VEGF gene therapy induced only a slight increase in VEGF blood concentrations.[16] In addition, overexpression of VEGF produces abnormal vessels in tumor angiogenesis.[17] These results suggest that in the context of ischemia, it is difficult to site-specifically modulate the concentration of a VEGF-related therapeutic to an appropriate value. Therefore, next-generation therapies targeting VEGFR, in addition to VEGF, may effectively induce site-specific angiogenesis for the treatment of ischemic disease. The novel in vivo imaging technique described here for the analysis of ischemic model mice may increase the understanding of the mechanisms of angiogenesis and aid in the development of VEGFR-related therapies.

Acknowledgments

The authors thank Yohei Hamanaka, Takayuki Nakagawa, Masaaki Kawai, and Makoto Hikage for helpful discussion and Yayoi Takahashi and Yasuko Furukawa for technical assistance.

This work was supported by the Japan MEXT (Grants-in-Aid for Scientific Research in Priority Areas; N.O. and K.G.), a Grant-in-Aid for a Research Project, Promotion of Advanced Medical Technology (H18-Nano-001) from the Ministry of Health, Labor and Welfare of Japan (N.O.), and Research for Promoting Technological Seeds of JST (K.G.). This work was also supported by the Biomedical Research Core of Tohoku University Graduate School of Medicine, Tohoku University Global COE Program "Global Nano-Biomedical Engineering Education and Research Network Center," Core Research for Evolutional Science and Technology of JST, and Konica Minolta Medical & Graphic Inc.

Authorship

Contribution: Y.H. and K.G. designed and performed the research, analyzed the data, and wrote the manuscript; M.T., A.S., and N.O. performed research and analyzed data; M.W. and S.S. performed research; and T.Y. provided the equipment for laser Doppler perfusion imaging and performed research.

Conflict-of-interest disclosure: K.G. and M.T. have received a research grant from Konica Minolta Medical & Graphic Inc. N.O. has received research grants from Takeda Pharmaceutical Company Limited and Konica Minolta Medical & Graphic Inc. The remaining authors declare no competing financial interests.

Correspondence: Kohsuke Gonda, Department of Nano-Medical Science, Graduate School of Medicine, Tohoku University, Seiryo-machi, Aoba-ku, Sendai 980-8575, Japan; e-mail: gonda@med.tohoku.ac.jp.

References

1. Simons M. Angiogenesis: where do we stand now? *Circulation.* 2005;111(12):1556-1566.
2. Carmeliet P. Angiogenesis in life, disease and medicine. *Nature.* 2005;438(7070):932-936.
3. Helisch A, Schaper W. Arteriogenesis: the development and growth of collateral arteries. *Microcirculation.* 2003;10(1):83-97.
4. Simons M, Ware JA. Therapeutic angiogenesis in cardiovascular disease. *Nat Rev Drug Discov.* 2003;2(11):863-871.
5. Gowdak LHW, Poliakova L, Wang XT, et al. Adenovirus-mediated VEGF(121) gene transfer stimulates angiogenesis in normoperfused skeletal muscle and preserves tissue perfusion after induction of ischemia. *Circulation.* 2000;102(5):565-571.
6. Lu YX, Shansky J, Del Tatto M, Ferland P, Wang XY, Vandenburgh H. Recombinant vascular endothelial growth factor secreted from tissue-engineered bioartificial muscles promotes localized angiogenesis. *Circulation.* 2001;104(5):594-599.
7. Sakr Y. Techniques to assess tissue oxygenation in the clinical setting. *Transfus Apher Sci.* 2010;43(1):79-94.
8. Gonda K, Watanabe TM, Ohuchi N, Higuchi H. In vivo nano-imaging of membrane dynamics in metastatic tumor cells using quantum dots. *J Biol Chem.* 2010;285(4):2750-2757.
9. Tada H, Higuchi H, Wanatabe TM, Ohuchi N. In vivo real-time tracking of single quantum dots conjugated with monoclonal anti-HER2 antibody in tumors of mice. *Cancer Res.* 2007;67(3):1138-1144.
10. Couffinhal T, Silver M, Zheng LP, Kearney M, Witzenbichler B, Isner JM. Mouse model of angiogenesis. *Am J Pathol.* 1998;152(6):1667-1679.
11. Limbourg A, Korff T, Napp LC, Schaper W, Drexler H, Limbourg FP. Evaluation of postnatal arteriogenesis and angiogenesis in a mouse model of hind-limb ischemia. *Nat Protoc.* 2009;4(12):1737-1748.
12. Hikage M, Gonda K, Takeda M, et al. Nano-imaging of the lymph network structure with quantum dots. *Nanotechnology.* 2010;21:18.
13. Carmeliet P, De Smet F, Loges S, Mazzone M. Branching morphogenesis and antiangiogenesis candidates: tip cells lead the way. *Nat Rev Clin Oncol.* 2009;6(6):315-326.
14. Gerhardt H, Golding M, Fruttiger M, et al. VEGF guides angiogenic sprouting utilizing endothelial tip cell filopodia. *J Cell Biol.* 2003;161(6):1163-1177.
15. Lu EX, Wagner WR, Schellenberger U, et al. Targeted in vivo labeling of receptors for vascular endothelial growth factor: approach to identification of ischemic tissue. *Circulation.* 2003;108(1):97-103.
16. Tongers J, Roncalli JG, Losordo DW. Therapeutic angiogenesis for critical limb ischemia: microvascular therapies coming of age. *Circulation.* 2008;118(1):9-16.
17. Jain RK. Normalization of tumor vasculature: an emerging concept in antiangiogenic therapy. *Science.* 2005;307(5706):58-62.

33rd Annual International Conference of the IEEE EMBS
Boston, Massachusetts USA, August 30 - September 3, 2011

Methods for Assessment of Effects of Habitual Exercise on the Autonomic Nervous Function Using Plethysmogram

Makoto Yoshizawa, *Member, IEEE*, Norihiro Sugita, Tomoyuki Yambe, *Member, IEEE*, Satoshi Konno, Telma Keiko Sugai, *Student Member, IEEE*, Makoto Abe, Noriyasu Homma, *Member, IEEE*

***Abstract*—The present paper has proposed two methods for obtaining the linear correlation of the baroreflex system without measurement of blood pressure. One is based on the pulse wave transit time which needs both the electrocardiogram and the photoplethysmogram. The other is based on the photoplethysmogram only. The results from the experiments showed that the effect of habitual exercise and the Valsalva maneuver can be verified quantitatively. The proposed methods are possible to be used for a test of the autonomic nervous function at home.**

I. Introduction

JAPAN is being a super-aging society, and thus the inflation of nationwide medical cost can be predicted exactly in the very near future. To prevent the crisis in the nation's deficit-ridden health insurance system, we should seriously consider some strategies for protecting people's health.

In this situation, one of the most effective methods is to entrench people to exercise habitually, which may be valid especially for people suffering from metabolic syndrome instructed to the specific medical checkup. To promote habitual exercise, some indices representing the effect of exercise should be fedback to the person after the exercise.

It has been indicated that the index corresponding to linear correlation of the baroreflex system is useful for expressing the autonomic nervous function [1,2]. We adopted this index as information fedback to the person exercising to settle it a habit.

Unfortunately this index needs measurement of continuous blood pressure to calculate. However it is not easy to measure continuous blood pressure because its sensor is too expensive and bulky to use at an ordinary home.

In this article, two alternative methods without measuring continuous blood pressure are introduced. One is a method in which the pulse wave transit time (PTT [ms]) is used instead of continuous blood pressure, and PTT is obtained from electrical cardiogram (ECG) and photoplethysmogram (PPG). The ECG is also difficult to measure at home and should not be used if possible. The other method does not need the ECG signal but linear correlation can be still obtained on the basis of only PPG signal.

In the use of these methods, the effect of habitual exercise on the index was evaluated and Valsalva maneuver was employed to ascertain the capability of the proposed method to extract individual difference from the calculated index.

Manuscript received April 15, 2011. This work was supported by the Sendai Area Knowledge Cluster Initiative founded by Japanese Ministry of Education, Science, Sports and Culture.

M. Yoshizawa and N. Homma are with the Research Division on Advanced Information Technology, Cyberscience Center, Tohoku University, 6-3 Aoba, Aramaki, Aoba-ku, Sendai, 980-8578 Japan (Corresponding author: M. Yoshizawa to provide phone: +81-22-795-3407 Ext. 838; e-mail: yoshizawa@isc.tohoku.ac.jp).

T. Yambe and S. Konno are with the Institute of Development, Aging and Cancer, Tohoku University, Sendai, 980-8575 Japan.

N. Sugita and M. Abe are with Graduate School of Engineering, Tohoku University, Sendai 980-8579, Japan.

T. K. Sugai is with Graduate School of Biomedical Engineering, Tohoku University, Sendai 980-8579, Japan.

II. Methods

A. Method Based on Pulse Wave Transit Time

Monitoring device

For home use, a measurement device should be wireless with less constraint. There are many monitoring systems but RF-ECG (Micro Medical Device, Inc.) is unique as a very small (40mm×35mm×7.4mm) and light (11.8g including electrical cell) wireless monitoring sensor to measure not only ECG but also acceleration and temperature as shown in Fig.1a).

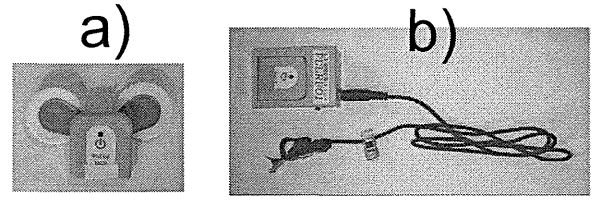

Fig. 1 Wireless sensors for measuring a) ECG signal and b) photo-plethysmographic signal

However, there is no small sized wireless device which can measure both ECG and PPG signals. In this study, we developed a sensor based on RF-ECG whose input terminal can acquire the PPG signal by attenuating its voltage level as shown in Fig.1b). To avoid the effect of body motion, the PPG signal was measured at the ear lobe and the sensor itself was inserted into a pocket on the chest of the subject's cloth. Another RF-ECG was used simultaneously to measure the ECG signal. Thus, both ECG and PPG signals can be measured in a wireless fashion at the sampling rate of 204Hz with less restriction.

The heart rate HR [bpm] was obtained from the reciprocal of the ECG signal, and PTT was calculated as the interval from the peak time of R-wave of the ECG signal

to the peak time of the velocity of the PPG signal. Both PTT and HR were band-pass filtered with a pass band between 0.08Hz and 0.12Hz to be limited to the Mayer wave-related frequency components. After the processing, cross-correlation coefficient $\rho(\tau)$ between these signals was calculated time-discretely as follows:

$$\rho(\tau) = \frac{\phi_{PTT,HR}(\tau)}{\sqrt{\phi_{PTT,PTT}(0) \cdot \phi_{HR,HR}(0)}} \qquad (1)$$

where $\phi_{PTT,HR}(\tau)$ is the cross-correlation function between PTT and HR, and $\phi_{PTT,PTT}(\tau)$ and $\phi_{HR,HR}(\tau)$ are auto-correlation functions of PTT and HR, respectively. In this study, $\rho(3)$, i.e., the value of $\rho(\tau)$ at $\tau = 3$ s was obtained as an index which represents the linear correlation of the baroreflex system from PTT to HR. The index $\rho(3)$ is more stable value than the conventional index $\rho_{\max}$ which is defined as the maximum value of $\rho(\tau)$ in spite of its lower value.

Experiment

In the experiment, elderly people were used as test subjects classified into two groups. One is the Exercise Group consisting of 8 healthy people (age 52 to 73; mean 65.6±7.7; 4 males and 4 females) exercising habitually for over 15min a week. The other is the Control Group consisting of 8 almost healthy people (age 55 to 75; mean 67.6±6.5; 3 males and 5 females) exercising little

To give dynamic change in subject's hemodynamics by using change in his or her posture, the experimental protocol was as follows:

1) Supine position (5 min)
2) Upright standing position (2 min)
3) Supine position (3 min)
4) Upright standing position (2 min)
5) Supine position (3 min)

B. . Method Based Only on Photoplethysmogram

Estimation of cross-correlation function

So far, many methods for obtaining blood pressure based on photoplethysmogram have been proposed, in which, for example, local maximum or minimum values of the acceleration of the signal are utilized. The purpose of these methods is usually to obtain the absolute value of blood pressure. However, if the purpose is to estimate the linear correlation of the baroreflex system, we can do it as shown below.

First, as shown in Fig.2, obtain the feature variables specifying the PPG signal at a certain beat such as the first extremum a and the second extremum b of the acceleration, the second extremum B of the velocity, the mean value MP and the difference PA between the maximum and minimum values of the signal within the beat. Since these variables are sampled every unequally-spaced interval, resample it every equally-spaced interval of 0.2s (5Hz) after the cubic spline interpolation. Let k be a discrete time which is incremented with the resampling, and produce a feature vector given by

$$x(k) = [a, b, b/a, a^2, b^2, ab, B/a, MP, PA]^T \qquad (2)$$

Consider a multiple regression model in which an explanatory variable is $x(k)$ and an objective variable is heart rate $y(k)$ as follows:

$$\hat{y}(k) = \beta^T x(k) + \varepsilon(k) \qquad (3)$$

where β is a coefficient vector to be identified with the least square method and $\varepsilon(k)$ is a residue. In general, it is expected that cross-correlation between blood pressure and heart rate whose frequency components are limited to the Mayer wave-related band is maximized a few second later. This phenomenon means that the baroreflex system has a delay. Let denote the delay as L [ms]. Unfortunately, the value of L is changed with time and subjects. Thus, find the optimal values β^* and L^* corresponding to β and L, respectively, so that the error between the $\hat{y}(k)$ and $y(k)$ can be minimized.

Instead of the value of (1), calculate a surrogate value that is obtained by letting $PTT = \hat{y}(k)$ and $HR = y(k)$ in (1). In this case, heart rate $HR = y(k)$ is calculated from the foot-to-foot interval (FFI [ms]) of the PPG.

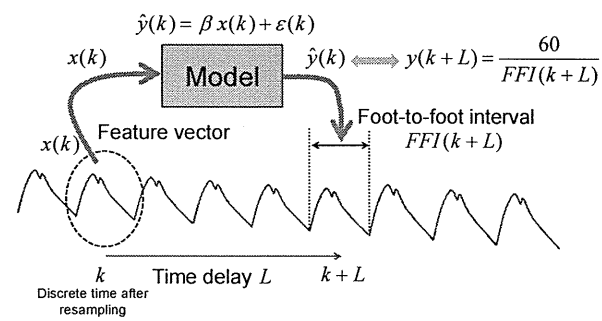

Fig.2 Multiple regression model with the input feature vector of pulse wave for estimation of heart rate.

The reason why the cross-correlation between heart rate and its estimate can be substituted by that between blood pressure and heart rate is shown below. It is known that heart rate correlates closely with blood pressure in the Mayer wave-rerated band at a resting state. If the output of the multiple regression model agrees well with the actual blood pressure, it is likely that the estimate obtained from the model also correlates well with heart rate.

On the other hand, the other method for estimation of blood pressure based on the PPG needs same calibration process using a blood pressure sensor. However, the proposed method employs the subject's heart rate as a reference value to identify the model parameters and does not needs any blood pressure sensor. While the method described in 2.1 which uses the PTT requires the ECG sensor

to specify the position of the R-wave, the proposed method uses only the PPG sensor which is cheap and expected to be widely spread.

Estimation of cross-correlation function

Thirty-two healthy subjects (Age 23.1±3.6; 24 males; 8 females) were used in an experiment including the Valsalva maneuver with a protocol as follows:

1) Rest (5 min)
2) Respiration cease (1 min)
3) Rest (3 min)
4) Respiration cease (1 min)
5) Rest (5 min)

A photo sensor and an amplifier for (BIOPAC; PPG100C) was used to measure the PPG signal at the index finger and blood pressure sensor (Finapres; Portapres) was used to measure continuous blood pressure at the middle finger.

III. . Results and Discussion

A. . Method Based on Pulse Wave Transit Time

Figure 3 shows a subject's data (Age 70; female; systolic/diastolic pressure=136mmHg/84mmHg) who was a member of the Exercise Group. The data are time courses of heart rate, HR, the normalized PTT to have zero mean and unit standard deviation, and the cross-correlation coefficient at $\tau = 3$, $\rho(3)$. At two parts of the upright standing position, HR increased like a rectangular shape, which corresponds to normal orthostatic baroreflex to regulate blood pressure. It is found that PTT also increased in the similar manner as HR but their shapes are not so similar. Decrease in $\rho(3)$ can be seen at the two parts around upright standing positions.

Figure 4 shows another subject's data (Age 72; female; systolic / diastolic pressure= 155mmHg / 102mmHg) who was a member of the Control Group. Unlike Fig.4, hear rate HR changed irregularly, which means the baroreflex did not work well. Moreover, the shape of PTT is very similar to that of HR. This fact may be caused by arterial sclerosis since she had light hypertension and she was taking depressor drug routinely. That is to say, the change in HR may be equal to that of PTT if blood vessel is like a lead pipe with less compliance. The absolute value of $\rho(3)$ was small and drifted around zero during the experiment, which implies that the regulation function manipulating HR based on blood pressure with 3 seconds delay was not well done by the autonomic nervous system.

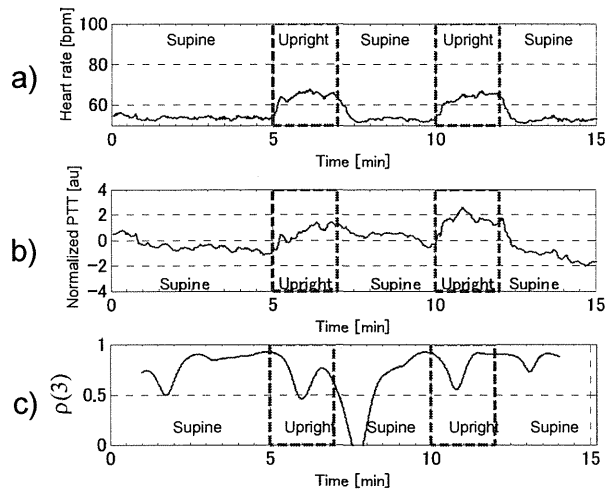

Fig.3 a)heart rate, b)normalized PTT and c)cross-correlation function $\rho(3)$ of a subject belonging to the Exercise Group (female; age 70; Systolic / diastolic pressure = 136mmHg/84mmHg).

Figure 5 shows the comparison of the mean value $\rho(3)$ between the Exercise and the Control Groups. It is found that the recovery speed of $\rho(3)$ of the Control Group was significantly lower than that of the Exercise Group in the interval between two upright standing positions. It can be guessed that this difference was caused by the effect of habitual exercise.

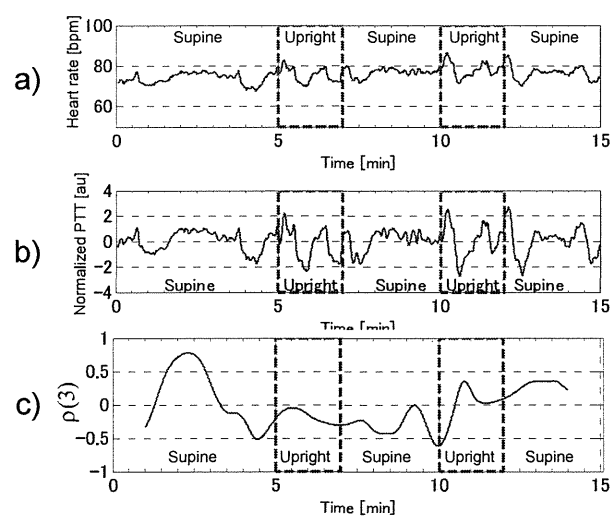

Fig.4 a)heart rate, b)normalized PTT and c)cross-correlation function $\rho(3)$ of another subject belonging to the Control Group (female; age 72; Systolic / diastolic pressure = 155mmHg /102mmHg).

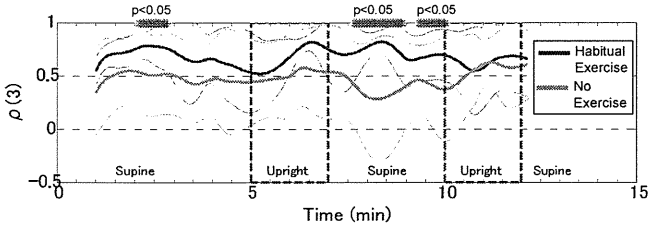

Fig.5 Comparison of $\rho(3)$ between the Exercise Group (n=8) and the Control Group (n=8). Solid line: mean. Broken line: S.D.

B. . Method Based Only on Photoplethysmogram

The mean value of thirty-two subjects' $\rho(3)$ obtained from the method based only on the PPG signal described in 2.2 are shown in Fig.6, accompanied by $\rho(3)$ calculated directly from measured blood pressure. The figure indicates that $\rho(3)$ based on the PPG is much lower than $\rho(3)$ based on the blood pressure and that the effect of respiration cease on the time trajectories was not clear in both two kinds of $\rho(3)$ s. The reason is that the data shown in Fig.6 includes the subjects whose $\rho(3)$ is low even in the resting state. It can be guessed that such subjects tend to have a dull autonomic nervous reflex function against the respiration cease.

Thus, the subjects were selected under the condition that the mean value of $\rho(3)$ in the resting state from 0min to 4min was higher than 0.5. There were 9 subjects who satisfy the condition, and the mean value of $\rho(3)$ of these subjects is shown in Fig.7. It seems that the decrease in $\rho(3)$ around the positions of the respiration cease got deep.

In the same way, when the threshold to select the subjects was increased to 0.7, four subjects survived and their mean value of $\rho(3)$ was shown in Fig.8. It can be found that the depth of the decrease around the respiration cease tended to get deeper and that the value of $\rho(3)$ based on the PPG in the resting state came closer to that based on the blood pressure.

These results suggest that the temporal change in the linear correlation of the baroreflex system can be estimated on the basis of the PPG signal only without measurement of the ECG or blood pressure. Moreover, it is possible that $\rho(3)$ based on the PPG is more sensitive to the effect of the respiration cease than $\rho(3)$ based on blood pressure.

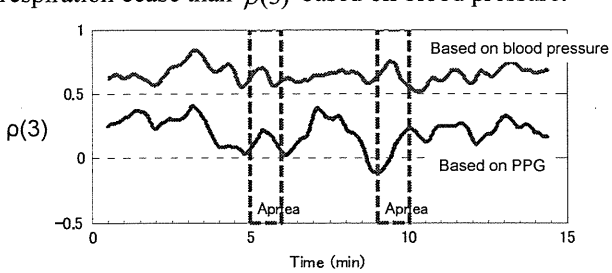

Fig. 6 Mean value of $\rho(3)$ over all 32 subjects.

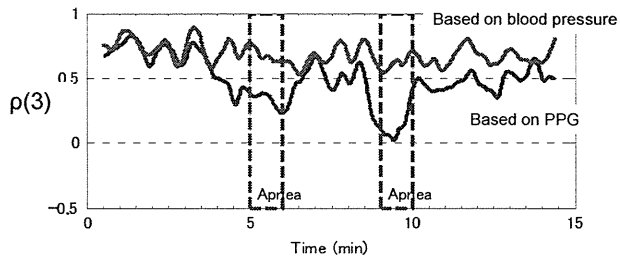

Fig.7 Mean value of $\rho(3)$ over 9 subjects whose mean value is larger than 0.5 from 0min to 4min.

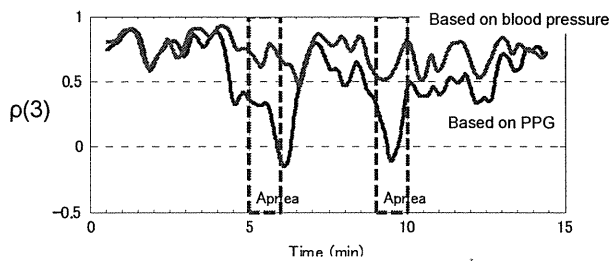

Fig.8 Mean value of $\rho(3)$ over 4 subjects whose mean value is larger than 0.7 from 0min to 4min.

IV. Conclusions

The present study has developed two methods for obtaining the linear correlation of the baroreflex system without measurement of blood pressure. One is based on the pulse wave transit time which needs both the ECG signal and the photoplethysmogram. The other is based on the photoplethysmogram only. The results from the experiment with the former method showed that the effect of habitual exercise can be verified quantitatively. The latter method indicated that the response of the linear correlation to the Valsalva maneuver can be estimated. The proposed methods are possible to be used for a test of the autonomic nervous function easily even at home.

Acknowledgment

The authors thank U-Medica Ink., ICR Co., Sendai City and Miyagi Prefecture collaborating with the Sendai Area Knowledge Cluster Initiative.

References

[1] Yoshizawa M, Sugita N, Tanaka A, Abe K, Yambe T, Nitta S: Quantitative and physiological evaluation of three dimensional images. Proceeding of the 7th International Conference on Virtual Systems and Multimedia: pp. 864-871, 2001

[2] Sugita N, Yoshizawa M, Abe M, et al: Evaluation of adaptation to visually induced motion sickness based on the maximum cross-correlation between pulse transmission time and heart rate, Journal of NeuroEngineering and Rehabilitation, vol. 4, no. 35, (Online Journal), 2007 (http:// www. jneuroengrehab. com/ content/ pdf/ 1743-0003-4-35.pdf)

Numerical Analysis of Effects of Measurement Errors on Ultrasonic-Measurement-Integrated Simulation

Kenichi Funamoto*, Toshiyuki Hayase, Yoshifumi Saijo, and Tomoyuki Yambe

Abstract—**Ultrasonic-measurement-integrated (UMI) simulation, in which feedback signals are applied to the governing equations based on errors between ultrasonic measurement and numerical simulation, has been investigated for reproduction of the blood flow field. However, ultrasonic measurement data inherently include some errors. In this study, the effects of four major measurement errors, namely, errors due to Gaussian noise, aliasing, wall filter, and lack of data, on UMI simulation were examined by a numerical experiment dealing with the blood flow field in the descending aorta with an aneurysm, the same as in our previous study. While solving the governing equations in UMI simulation, Gaussian noise did not prevent the UMI simulation from effectively reproducing the blood flow field. In contrast, aliasing caused significant errors in UMI simulation. Effects of wall filter and lack of data appeared in diastole and in the whole period, respectively. By detecting significantly large feedback signals as a sign of aliasing and by not adding feedback signals where measured Doppler velocities were aliasing or zero, the computational accuracy substantially improved, alleviating the effects of measurement errors. Through these considerations, UMI simulation can provide accurate and detailed information on hemodynamics with suppression of four major measurement errors.**

Index Terms—**Biofluid mechanics, computational fluid dynamics, measurement-integrated (MI) simulation, ultrasonic devices.**

I. Introduction

STRESSES due to blood flow on a blood vessel wall (hemodynamic stresses) are closely related to development and progression of circulatory diseases such as atherosclerosis and aneurysms. The results of *in vitro* cellular experiments [1], [2], animal experiments [3], [4], numerical simulations of blood flow [5], and comparison of those results with clinical findings [6], [7] have indicated the mechanisms of circulatory diseases. Especially, changes of state of endothelial cells by wall shear stress (WSS) have been intensively investigated, and some relationships between circulatory diseases and WSS have been proposed. For instance, low, oscillatory WSS causes atherosclerosis, and a bifurcation of an artery such as a carotid artery is well known as a likely site of atherosclerosis [8]. Concerning aneurysms, though there are conflicting suggestions that low/high WSS may lead to the ruptures [6], [7], WSS of physiologically abnormal magnitude is a possible trigger.

Among methods to measure blood flow field, ultrasonic measurement is characterized by noninvasive, real-time visualization of hemodynamics as well as blood vessel configuration by means of color Doppler imaging. In this method, pulses of ultrasound are transmitted from an ultrasound probe along scanning lines on a plane at a certain pulse repetition frequency (PRF), or a sampling frequency, and the echo from tissue is received with the same probe. Then, the magnitudes of the echo signals along the scanning lines are converted to brightness to visualize the tissue configuration, and the Doppler velocity is calculated from the Doppler shift frequency of the echo signal. Note that the Doppler velocity is the one-directional component of the velocity vectors along the ultrasonic beam, and practice and time are required to recognize the 3-D complicated hemodynamics. Moreover, hemodynamic stresses of WSS and pressure cannot be directly obtained with this method. On the other hand, numerical simulation of blood flow provides information on hemodynamic stresses as well as on the blood flow field [5]. Recently, fluid–structure interaction simulation enables investigation of the blood flow field considering the blood vessel wall motion due to its elasticity [9]. Numerical simulation essentially depends on boundary and initial conditions. However, it is difficult to precisely set these conditions in the numerical simulation of *in vivo* complicated unsteady blood flow [10], resulting in a computational result which may be different from the real blood flow.

Measurement-integrated (MI) simulation or a flow observer, which integrates measurement and numerical simulation, has been investigated as a methodology to overcome individual limitations in measurement and computation. Hayase and Hayashi [11] conducted a numerical experiment, showing that turbulent flow in a square duct was reproduced by MI simulation. Nisugi *et al.* [12] developed a hybrid wind tunnel, which integrated experimental wind tunnel measurement and numerical simulation, and analyzed a Karman vortex street behind a square cylinder. In addition, Yamagata *et al.* [13] performed MI simulation of the Karman vortex street with particle image velocimetry (PIV) measurement. Nakao *et al.* [14] fed back measurement data on velocity and pressure in an orifice to a numerical simulation with a k–ε turbulent model and achieved improvement of computational accuracy.

Manuscript received June 30, 2010; revised October 15, 2010; accepted November 11, 2010. Date of publication November 29, 2010; date of current version February 18, 2011. This work was supported in part by Grant-in-Aid for Young Scientists (start-up), Japan Society for the Promotion of Science (JSPS) (19860008), in part by a Grant-in-Aid for Young Scientists (B), Ministry of Education, Culture, Sports, Science, and Technology-Japan (MEXT) (21700459), and in part by Tohoku University Global COE (Center of Excellence) Program "Global Nano-Biomedical Engineering Education and Research Network Center." *Asterisk indicates corresponding author.*

*K. Funamoto and T. Hayase are with the Institute of Fluid Science, Tohoku University, Sendai 980-8577, Japan (e-mail: funamoto@reynolds.ifs.tohoku.ac.jp).

Y. Saijo is with the Graduate School of Biomedical Engineering, Tohoku University, Sendai 980-8579, Japan.

T. Yambe is with the Institute of Development, Aging and Cancer, Tohoku University, Sendai 980-8575, Japan.

Color versions of one or more of the figures in this paper are available online at http://ieeexplore.ieee.org.

Digital Object Identifier 10.1109/TBME.2010.2095418

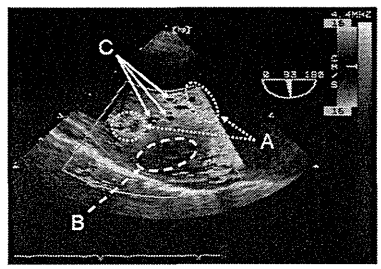

Fig. 1. Example of color Doppler imaging of a thoracic aneurysm in systole with indications of measurement errors. (A) Aliasing, (B) wall filter, and (C) lack of data.

As medical applications of MI simulation, the authors have proposed integration of medical measurement (ultrasonic measurement or MRI) of blood flow velocity and a numerical simulation to reproduce the blood flow field [15]–[17]. Ultrasonic-MI (UMI) simulation feeds back errors between measured and computed Doppler velocities to the numerical simulation to make the computational result converge to the real flow [16]. In our previous numerical experiments [15], [16], the efficiency of the UMI simulation was revealed, and the transient and steady characteristics of the method were investigated. In these studies, unsteady or steady numerical solution with realistic boundary conditions was first defined as the standard solution. Then, UMI simulation with inaccurate boundary conditions but with the same flow volume was evaluated as to how it reproduced the standard solution. In the feedback process, for purposes of simplicity, Doppler velocities of the standard solution were used without consideration of measurement errors.

Ultrasonic measurement of real *in vivo* blood flow inherently includes some measurement errors. Fig. 1 shows an example of a color Doppler image of an aneurysm in the descending aorta by means of transesophageal ultrasonography [18]. Noise is a cause of measurement error, adding some deviance to the Doppler velocity. Moreover, the settings of ultrasound Doppler measurement may cause measurement errors. The range of measurable Doppler velocity is defined by the PRF in the ultrasound Doppler measurement. In case the Doppler shift frequency exceeds half of the PRF, it is regarded as a frequency shift from a frequency different from the true one, resulting in aliasing, by which the Doppler velocity with incorrect direction and magnitude in regions with high blood flow velocity is provided (see "A" in Fig. 1). Color Doppler imaging utilizes a wall filter or a moving target indicator (MTI) filter which ignores the components of the Doppler shift frequency less than a certain value to distinguish tissue motion and blood flow. This filtering is effective for extracting blood vessel configuration, but it incidentally provides zero velocity in regions with slow blood flow velocity in a blood vessel (see "B" in Fig. 1). Furthermore, measurement data may be lacking at measurement points when the intensity of echo signals from blood cells is too small or when artifacts occur (see "C" in Fig. 1).

Feedback using measurement data with the aforementioned measurement errors may lead to UMI simulation with computational results different from the real blood flow field. Hence, this study investigated the effects of four major measurement errors, i.e., errors due to noise (Gaussian noise), aliasing, wall filter, and lack of data, on the UMI simulation by a numerical experiment dealing with a 3-D unsteady blood flow field in a descending aorta with an aneurysm, the same as in our previous study [16]. The treatments for each measurement error are also discussed.

TABLE I
CLASSIFICATION OF STANDARD SOLUTION (SS), ORDINARY SIMULATION (OS), AND UMI SIMULATION (UMIS)

Name	Inlet	Outlet	Feedback
SS	realistic velocity profile	realistic velocity profile	No
OS	uniform velocity profile	free flow	No
UMIS	uniform velocity profile	free flow	Yes

II. METHODS

It is difficult to obtain 3-D information on the blood flow field by measurement, though such information is indispensable to evaluate computational accuracy of UMI simulation. Consequently, effects of measurement errors on UMI simulation were investigated by applying the methods employed in our previous numerical experiment dealing with a 3-D unsteady blood flow field in an aneurysm [16]. A numerical solution of blood flow simulation obtained with realistic boundary conditions was first defined as the standard solution or a model of real flow, and the Doppler velocities corresponding to an ideal measurement data were obtained. For the Doppler velocities of the standard solution, one of four measurement errors due to Gaussian noise, aliasing, wall filter or lack of data was introduced. Assuming that the exact boundary conditions were unknown, a UMI simulation and an ordinary simulation were performed with inaccurate boundary conditions. For the UMI simulation, a feedback signal was applied using the Doppler velocity of the standard solutions with/without measurement errors. The computational accuracy of each UMI simulation was evaluated as to reproduction of the original standard solution, compared with that of an ordinary simulation without feedback. Table I summarizes the computational simulations conducted in this study.

A. UMI Simulation

Governing equations of UMI simulation of blood flow are the Navier–Stokes equations for incompressible and viscous fluid flow

$$\rho\left(\frac{\partial \mathbf{u}}{\partial t}+(\mathbf{u}\cdot\nabla)\,\mathbf{u}\right)=\mu\Delta\mathbf{u}-\nabla p+\mathbf{f} \tag{1}$$

and the pressure equation

$$\Delta p=-\nabla\cdot\rho\,(\mathbf{u}\cdot\nabla)\,\mathbf{u}+\nabla\cdot\mathbf{f} \tag{2}$$

where ρ and μ are, respectively, the density and viscosity of blood, t is time, $\mathbf{u}=(u,\,v,\,w)$ is the velocity vector, and p is the pressure. $\mathbf{f}=(f_x,\,f_y,\,f_z)$ denotes the artificial body force or the feedback signal which is applied at feedback points defined in a feedback domain. The pressure equation, (2), is derived by substituting the equation of continuity into the divergence of the Navier–Stokes equation, Eq. (1).

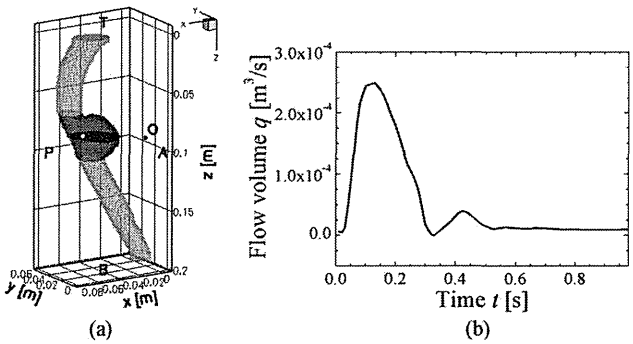

Fig. 2. (a) Computational domain with a feedback domain (gray zone), a probe position at O, and a monitoring point (white dot), and (b) variation of flow volume in one cardiac cycle.

The feedback signal in UMI simulation is defined as being proportional to the optimal estimation of the difference in velocity vector obtained by Doppler velocities by means of ultrasonic measurement and the numerical simulation

$$\mathbf{f} = -K_{\mathrm{v}}^{*} \frac{\Phi_d \left(\mathbf{u}_{\mathrm{c}} - \mathbf{u}_{\mathrm{s}}\right)}{U} \left(\frac{\rho U^2}{L}\right) \tag{3}$$

where K_{v}^{*} is the feedback gain (nondimensional), U is the characteristic velocity, L is the characteristic length, $\mathbf{u}_{\mathrm{c}}$ and $\mathbf{u}_{\mathrm{s}}$ are velocity vectors of the computational result and the standard solution (or real flow), respectively, and Φ_d ($d = 1, 2, 3$) is a projection function of a 3-D vector to the d-dimensional subspace generated by the vectors of the ultrasonic beam directions. Note that the special case with $K_{\mathrm{v}}^{*} = 0$ is an ordinary numerical simulation without feedback. The acquisition of Doppler velocity by projecting a velocity vector in the direction of the ultrasonic beam corresponds to the case of $d = 1$. In numerical simulation, all parameters are nondimensionalized by characteristic values. Reference length, L, and reference velocity, U, are the entrance diameter of the blood vessel, D, and mean inlet velocity at peak flow, $u'_{\max}$, respectively, and blood density ρ is used as the reference density. The above governing equations are discretized and solved by means of the finite volume method. Feedback signals are updated and added at each iteration step using the latest velocity results. For detailed descriptions of the projection function, Φ_d, and discretization, see our previous study [16].

B. Procedure of Numerical Experiment

Every setting to obtain the standard solution and to perform the UMI simulation was the same as that in the previous study [16]. Briefly, the objective was the blood flow in a chronic aortic aneurysm in the descending aorta in a 76-year-old female patient, who had no significant complications (see Fig. 2(a)). The configuration of the whole aorta from the ascending aorta to the abdominal aorta including the aneurysm was reconstructed by accumulating the X-ray CT images (AquilionTM 16, Toshiba, Tokyo, Japan) with commercial 3-D reconstruction software (Mimics 7.3, Materialise, Leuven, Belgium). All computations were performed in the computational domain shown in Fig. 2(a) with an original program similar to the SIMPLER method. In the computational program, a consistently reformulated QUICK scheme was used for discretization of the convective terms in Navier–Stokes equations, and a second-order implicit scheme was employed for that of time derivative terms [16]. The computational grid consisted of an orthogonal equidistant staggered grid system with $43 \times 30 \times 91$ grid points in the x, y, and z directions, respectively. First, we performed a computation to obtain the standard solution by applying unsteady velocity profiles at the upstream and downstream boundaries. These boundary conditions were obtained from a preliminary simulation in the whole aorta, including the present domain by using commercial computational fluid dynamics software (FLUENT 6.1.22, Fluent, Inc., Lebanon, NH). This is because the orthogonal grid system of the present scheme is not efficient for the analysis of the whole aorta domain. Zero velocity was assumed on the wall. Seventy percent of the cardiac output of 7.0×10^{-5} m^3/s (4.2 l/min) was assumed to flow through the blood vessel. The heart rate was 61 bpm (1.02 Hz), so that one cardiac cycle was $T^{*} = 0.98$ s. The variation of blood flow volume was provided with reference to [19], as shown in Fig. 2(b). The inlet diameter of the blood vessel, D ($=L$), was 29.25×10^{-3} m, and the mean inlet velocity at peak flow, $u'_{\max}$ ($=U$), was 36.70×10^{-2} m/s. Consequently, the reference time T ($=D/U$) was 7.97×10^{-2} s. The density and viscosity of blood were set at $\rho = 1.00 \times 10^3$ kg/m^3 and $\mu = 4.00 \times 10^{-3}$ Pa·s, respectively, within the normal range. The computational time step sufficient to obtain an accurate result was $\Delta t = 0.01$ s (0.125, nondimensionally) as shown by test computations.

A former study dealing with reproduction of 3-D steady flow revealed that the positioning of an ultrasound probe affected the computational result of the UMI simulation, and that using such a probe at the same height of an aneurysm yields the best reduction of the error in the velocity field in the aneurysmal domain and a fast response to the targeted steady state of the blood flow field [15]. Hence, in the UMI simulation, one probe was located at the point O [$(x, y, z) = (0.49, 0.00, 2.94)$ ((0.014 m, 0.000 m, 0.086 m), dimensionally)] in Fig. 2(a) for the acquisition of Doppler velocities at all the grid points in the fluid region of domain M [$2.26 \leq z \leq 3.62$ (0.066 m $\leq z \leq$ 0.106 m, dimensionally), shown by dark gray in Fig. 2(a)], which covered the whole aneurysmal domain, including the parent blood vessel. To obtain information on Doppler velocities in domain M, transesophageal ultrasonography with rotation of the beam plane was assumed. Regarding the boundary conditions, the exact boundary conditions for the standard solution were assumed to be unknown, and the UMI simulation was carried out with simple boundary conditions: zero velocity on the wall, an unsteady parallel flow with a uniform velocity profile at the inlet, and a free flow condition ($\partial/\partial n = 0$, n: coordinate normal to the boundary) at the outlet with the same flow volume as the standard solution in Fig. 2(b) (see Table I). Concerning the initial condition, UMI simulation in this study started from a zero velocity field. Though the inaccurate boundary conditions introduced error to the blood flow field in the aneurysm, the addition of feedback signals at the feedback points worked to reduce the error in the UMI simulation.

C. Introduction of Measurement Error

In order to evaluate the effects of measurement errors on the UMI simulation, Doppler velocities of the standard solution with one of four measurement errors of noise, aliasing, wall filter, and lack of data were individually used for feedback. For the introduction of the measurement error, a measurable Doppler velocity range, which was determined by the PRF in ultrasound Doppler measurement, was referred to. Generally, for color Doppler imaging of blood flow in the descending aorta by transesophageal ultrasonography, the Doppler velocity range (see a color bar in Fig. 1) is set to be relatively small since targeted blood flow is close to an ultrasound probe (see a probe position O in Fig. 2(a)). The typical measurable Doppler velocity range, $|V_0|$, for color Doppler imaging of the standard solution was thought to be within $|V_0| < 0.87$ (32 cm/s, dimensionally), referring to the incidence degrees of aliasing described later. The setting of a transesophageal ultrasound probe corresponds to a PRF of 3.7 kHz and a center frequency of 4.4 MHz [18]. Since it is difficult to specify the amounts of measurement errors, they were set in appropriate ranges.

1) Gaussian Noise: Doppler velocity can be different from the true value due to the effect of noise; ultrasound measurement provides Doppler velocity as a summation of the true value and some deviance

$$V' = V + \tilde{V}. \tag{4}$$

In this study, noise, assumed to follow the normal distribution $N(\mu_V, {\sigma_V}^2)$ with $\mu_V = 0$ and with four different values of the standard deviation, $\sigma_V = 0.011$, 0.022, 0.044, and 0.087 (0.4, 0.8, 1.6, and 3.2 cm/s, dimensionally), was respectively added to the Doppler velocity of the standard solution. For the sake of simplicity, the occurrence of aliasing was not considered in the process. Note that idealized ultrasonic measurement without noise corresponds to the case of $\sigma_V = 0$. The above settings were equivalent to the cases that deviances due to noise were 1.25%, 2.5%, 5%, and 10% values against the magnitude of the typical measurable Doppler velocity range of $|V_0| = 0.87$ (32 cm/s, dimensionally). For instance, variations of Doppler velocity of the standard solution at a monitoring point [$(x, y, z) = (1.84, 1.16, 2.94)$, ((0.054 m, 0.034 m, 0.086 m), dimensionally), a white dot in Fig. 2(a)] in the parent artery in one cardiac cycle in the cases of $\sigma_V = 0$, 0.022, and 0.087 are shown in Fig. 3. With increasing standard deviation, σ_V, deviance against the ideal ultrasonic measurement data ($\sigma_V = 0$) or the true Doppler velocity increases at each time moment. The effect of noise is relatively significant in diastole ($t/T^* > 0.4$) when the blood flow velocity itself is low.

2) Aliasing: PRF determines the range of measurable Doppler velocity. Doppler velocity whose magnitude exceeds that of the measurable Doppler velocity is folded and is recognized as velocity with incorrect magnitude and direction (see "A" in Fig. 1). Specifically, if the magnitude of Doppler velocity, V, exceeds that of the measurable Doppler velocity, $V_{\rm thre}$, V is provided as V' which is within $\pm|V_{\rm thre}|$ with the following

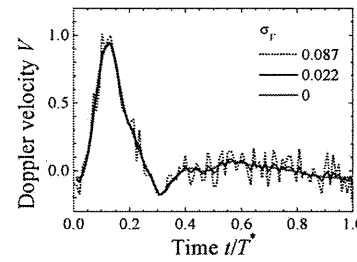

Fig. 3. Doppler velocity at a grid point, $(x, y, z) = (1.84, 1.16, 2.94)$ ((0.054 m, 0.034 m, 0.086 m) in dimensional values), with Gaussian noise with three different degrees of standard deviation, σ_V, in one cardiac cycle (nondimensional).

transformation:

$$V' = \begin{cases} 2|V_{\rm thre}| + V & (V < -|V_{\rm thre}|) \\ V & (|V| < |V_{\rm thre}|) \\ -2|V_{\rm thre}| + V & (|V_{\rm thre}| < V). \end{cases} \tag{5}$$

In this study, the threshold value, $|V_{\rm thre}|$, of measurable Doppler velocity was set at four different values of 0.22, 0.44, 0.87, or 1.09 (8, 16, 32, or 40 cm/s, dimensionally). Among them, color Doppler images with $|V_{\rm thre}| = 0.87$ well visualized both small and large Doppler velocities in the aneurysm in the cardiac cycle though some aliasing occurred. Hence, the setting of the threshold of Doppler velocity was considered as the normal setting, $|V_0|$. The percentage of points where aliasing occurred in the feedback points, $N_A/N_{\rm FB}$, at each time step is shown in Fig. 4(a). With decreasing measurable Doppler velocity range, aliased points increased. The timing of the maximum value of $N_A/N_{\rm FB}$ does not necessarily coincide with that of the maximum flow rate due to the relationship between an ultrasound beam angle and the vortex in the aneurysm ($t/T^* = 0.13$; see Fig. 2(a)).

3) Wall Filter: Generally, color Doppler imaging utilizes a wall filter, called an MTI filter, to distinguish blood flow and blood vessel wall motion. The filter enables the extraction of blood flow, but it tends to display slow Doppler velocities as zero near the blood vessel wall, in an aneurysm and at locations where blood flow direction is approximately perpendicular to the ultrasonic beam (see "B" in Fig. 1). To take the wall filter into account, Doppler velocities of the standard solution whose magnitudes were not larger than a threshold value, $|V_{\rm WF}|$, were zeroed as follows:

$$V' = \begin{cases} 0, & (|V| \le |V_{\rm WF}|) \\ V, & (|V| > |V_{\rm WF}|). \end{cases} \tag{6}$$

Considering that Doppler velocity being cut by the wall filter was 1.25%, 2.5%, 5%, or 10% of the measurable Doppler velocity, $|V_{\rm WF}|$ was, respectively, set at four different values of 0.011, 0.022, 0.044, or 0.087 (0.4, 0.8, 1.6, or 3.2 cm/s, dimensionally). Fig. 4(b) shows the percentage of feedback points, $N_{\rm WF}/N_{\rm FB}$, whose Doppler velocities of the standard solution were set to be zero. The number of filtered points increases in diastole since blood flow slows down (see Fig. 2(b)).

4) Lack of Measurement Data: In ultrasonic measurement, measurement data is sometimes lacking, being displayed as zero,

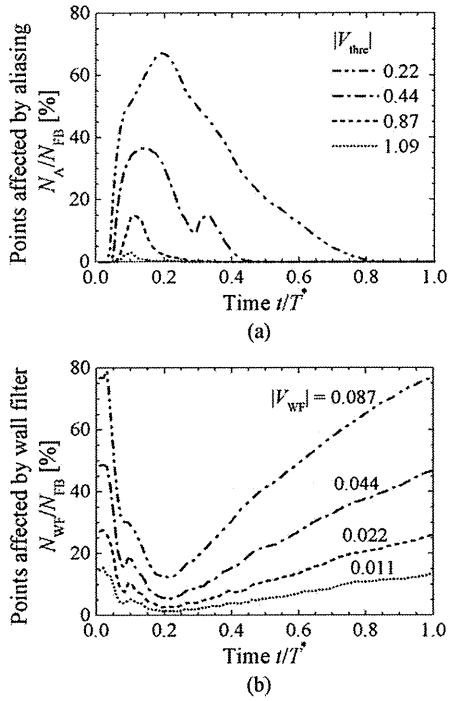

Fig. 4. Percentage of the number of grid points: (a) N_A and (b) N_{WF}, where the standard solution was affected by aliasing and wall filter, with respect to the total number of feedback points, N_{FB}, respectively.

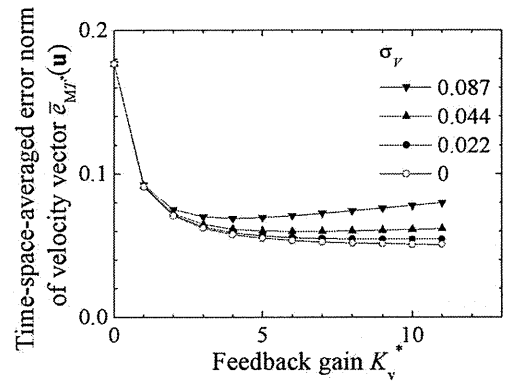

Fig. 5. Variation of time-space-averaged error norm of velocity vector of UMI simulation using the standard solution affected by Gaussian noise with feedback gain.

in cases in which the intensity of echo signals from blood cells is too small or artifacts are present (see "C" in Fig. 1). To examine the effect on UMI simulation, Doppler velocities at feedback points were randomly zeroed at a certain ratio at each time step and used for feedback. The ratio, $N_{\mathrm{LD}}/N_{\mathrm{FB}}$, of points whose Doppler velocities were lacking to all feedback points was set at four different values of $N_{\mathrm{LD}}/N_{\mathrm{FB}} = 1\%$, 5%, 10%, or 20%.

D. Error Evaluation Method

For the evaluation of the computational result, space-averaged and time-space-averaged error norms of velocity vector $\mathbf{u}$, $\bar{e}_{\mathrm{M}}(\mathbf{u}, t)$ and $\bar{e}_{MT^*}(\mathbf{u})$, based on the l_1 norm, $|u| + |v| + |w|$ for velocity vector $\mathbf{u}$ were calculated

$$\bar{e}_{MT^*}(\mathbf{u}) = \frac{1}{T^*}\int_{T^*} \bar{e}_{\mathrm{M}}(\mathbf{u}, t)dt = \frac{1}{T^*}\int_{T^*}\left(\frac{1}{N}\sum_n \frac{|\mathbf{u}_{cn}(t) - \mathbf{u}_{sn}(t)|}{U}\right)dt \quad (7)$$

where n and N are the index and the total number of monitoring points in the feedback domain M, respectively, and subscripts c and s, respectively, indicate the result of the UMI simulation and the standard solution. Error norms of Doppler velocity V, $\bar{e}_{\mathrm{M}}(V, t)$ and $\bar{e}_{MT^*}(V)$, were also defined in the same way.

III. Results and Discussion

The ability to reproduce the standard solution by UMI simulations with/without each measurement error compared with that of the ordinary simulation without feedback was evaluated (see Table I). In the UMI simulation using the standard solution without measurement errors, the time-space-averaged error norm of the velocity vector, $\bar{e}_{MT^*}(\mathbf{u})$, monotonically decreased with increasing feedback gain K_v^* at an interval of 1, but the computation diverged for $K_v^* \geq 12$ (see white circle symbols in Fig. 5). Consequently, in the absence of special notations, the computational results of the UMI simulations at $K_v^* = 11$ were basically used for evaluation of the computational accuracy.

A. Effect of Gaussian Noise

Variations of the time-space-averaged error norm of the velocity vector, $\bar{e}_{MT^*}(\mathbf{u})$, with feedback gain, K_v^*, in the UMI simulations using the standard solution with noise ($\sigma_V = 0.022$, 0.044, 0.087) are shown with black symbols in Fig. 5. The result at $K_v^* = 0$ is the ordinary simulation without feedback. Comparison of the results at the same feedback gain indicates that the computational accuracy deteriorates as the degree of noise increases. In addition, by using the standard solution with relatively large noise such as $\sigma_V = 0.087$, the computational accuracy of UMI simulation becomes worse with increasing feedback gain. However, within the degree of noise in this study, the error in the UMI simulation become smaller than that in the ordinary simulation ($K_v^* = 0$) in all conditions, implying the improvement of the computational accuracy.

For each UMI simulation using the standard solution with noises of $\sigma_V = 0.011$, 0.022, 0.044 and 0.087, optimum feedback gain, at which $\bar{e}_{MT^*}(\mathbf{u})$ became the smallest, was obtained as $K_v^* = 11$, 10, 6, and 4, respectively. Hereafter, in this subsection, the computational accuracy of the UMI simulation at each optimum feedback gain is investigated in greater detail. Fig. 6(a) compares space-averaged error norms of Doppler velocity, $\bar{e}_{\mathrm{M}}(V, t)$, between UMI simulations using the standard solution without noise ($\sigma_V = 0$, dotted line) and with noise of $\sigma_V = 0.044$ (dashed line), the standard solution with the noise of $\sigma_V = 0.044$ (gray line), and the ordinary simulation (black line). Deviances in Doppler velocity of the standard solution due to noise leads $\bar{e}_{\mathrm{M}}(V, t)$ of the UMI simulation to somewhat increase. However, the value is smaller than that of the ordinary simulation, showing that even the UMI simulation with noise

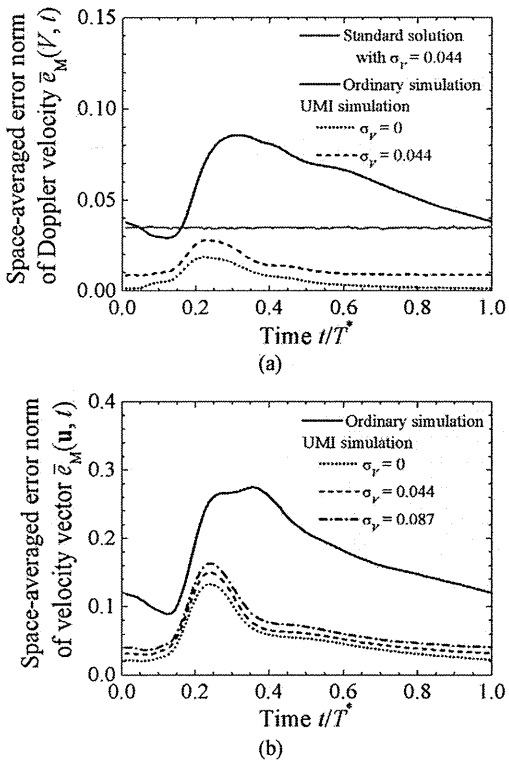

Fig. 6. Comparison of space-averaged error norms of (a) Doppler velocity and (b) of velocity vector among the standard solution affected by Gaussian noise, the ordinary simulation without feedback, and UMI simulations at each optimum feedback gain.

reduces error derived from inaccurate boundary conditions for the sake of feedback. More importantly, the value of $\bar{e}_M(V, t)$ of the UMI simulation (a dashed line in Fig. 6(a)) was smaller than that of the standard solution with noise itself (a gray line in Fig. 6(a)). This indicates the possibility that the UMI simulation provides a result close to the true Doppler velocity more precisely than the ultrasonic measurement affected by noise. Variations of space-averaged error norm of the velocity vector, $\bar{e}_M(\mathbf{u}, t)$, are shown in Fig. 6(b). At every time moment, the results of the UMI simulations are much smaller than that of the ordinary simulation, implying that the effect of noise included in the standard solution is minute.

The reason why the UMI simulation using the standard solution with Gaussian noise makes the computational result approach the true standard solution without deterioration of the computational accuracy is that the method calculates the velocity and pressure fields to satisfy the governing equations. The divergence of the feedback signals in the pressure equation of Eq. (2) does not become zero because of the noise included in the standard solution. However, components of the standard solution buried in the noise approach the above term zero and the result of the UMI simulation approaches the true standard solution. Therefore, even if noise included in the standard solution is applied for the feedback in the UMI simulation, it hardly influences the computational result.

As an example of visualization of the blood flow field, contours of Doppler velocity on multiple cross sections of the aneurysm and the parent artery at the timing of the maximum flow rate ($t/T^* = 0.13$ (0.13s)) are represented in Fig. 7. Because of the existence of a vortex in the aneurysm, velocity components of blood flow approaching and leaving an ultrasound probe exist, resulting in a mosaic pattern with warm and cold colors. Compared with the color Doppler image of the standard solution without measurement errors in Fig. 7(a), mottling can be observed in Fig. 7(b) under the influence of the noise ($\sigma_V = 0.087$). On the other hand, the color Doppler image of the UMI simulation in Fig. 7(c) has no mottling and resembles Fig. 7(a), though the standard solution with noise (see Fig. 7(b)) was used in the process of feedback.

B. *Effect of Aliasing*

This subsection discusses effect and treatment of aliasing in the UMI simulation. In Fig. 8(a), variations of time-space-averaged and space-averaged error norms of velocity vector, $\bar{e}_{MT^*}(\mathbf{u})$ and $\bar{e}_M(\mathbf{u}, t)$, with feedback gain (left figure) and with time (right figure) are compared between the UMI simulations using the standard solution with/without aliasing ($|V_{\mathrm{thre}}| = 0.22$, 0.44, 0.87 and 1.09) and the ordinary simulation without feedback ($K_v^* = 0$). In the case of $|V_{\mathrm{thre}}| = 0.22$, the error norm, $\bar{e}_{MT^*}(\mathbf{u})$, of the UMI simulation monotonically increases as the feedback gain increases (see the left figure in Fig. 8(a)). In cases that the measurable Doppler velocity range is relatively large ($|V_{\mathrm{thre}}| > 0.44$), the error norm of the UMI simulation in the proper condition is smaller than that of the ordinary simulation, even if aliasing occurs in the standard solution. Note that $\bar{e}_{MT^*}(\mathbf{u})$ evaluates the error of velocity vector by averaging in one cardiac cycle. Evaluation of the error at each time moment with the error norm of $\bar{e}_M(\mathbf{u}, t)$ shows that there are timings when the computational accuracy of the UMI simulation becomes worse than that of the ordinary simulation by using an aliased standard solution for feedback (see the right figure in Fig. 8(a)). As seen in the result of the case of $|V_{\mathrm{thre}}| = 1.09$, even though the duration of aliasing is short with a small percentage of aliased points in the feedback points (see Fig. 4(a)), instantaneous deterioration of the computational accuracy occurs in systole and the effect remains after that. Thus, the UMI simulation works to reproduce the aliasing included in the standard solution, and the computational accuracy becomes worse.

When aliased data is applied for feedback, the magnitude of feedback signal at the feedback point becomes abnormally large since the Doppler velocity drastically changes compared with those around the point. The authors have previously proposed a treatment method for aliasing in a study concerning two-dimensional UMI simulation of the blood flow field [20]. In this study, the treatment method was also examined in the 3-D UMI simulation, i.e., by detecting the cases of $|\Phi_1(\mathbf{u}_c - \mathbf{u}_s)| > |V_{\mathrm{thre}}|$, application of a feedback signal was cancelled at the feedback point. Error norms, $\bar{e}_{MT^*}(\mathbf{u})$ and $\bar{e}_M(\mathbf{u}, t)$, of the UMI simulation with the above treatment for aliasing are shown in Fig. 8(b). Compared with Fig. 8(a), the error norms decrease in all the cases, implying that the aliasing is successfully detected and canceled. The values of UMI simulations are almost the

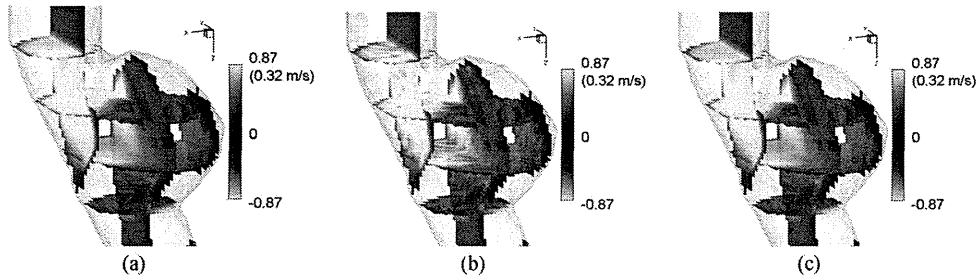

Fig. 7. Contour maps of Doppler velocity on four horizontal and three vertical planes at peak flow ($t/T^* = 0.13$): the standard solutions (a) without measurement errors and (b) with Gaussian noise of $\sigma_V = 0.087$ (3.2 cm/s in dimensional value), and the UMI simulation using the data "(b)" for feedback at $K_v^* = 11$.

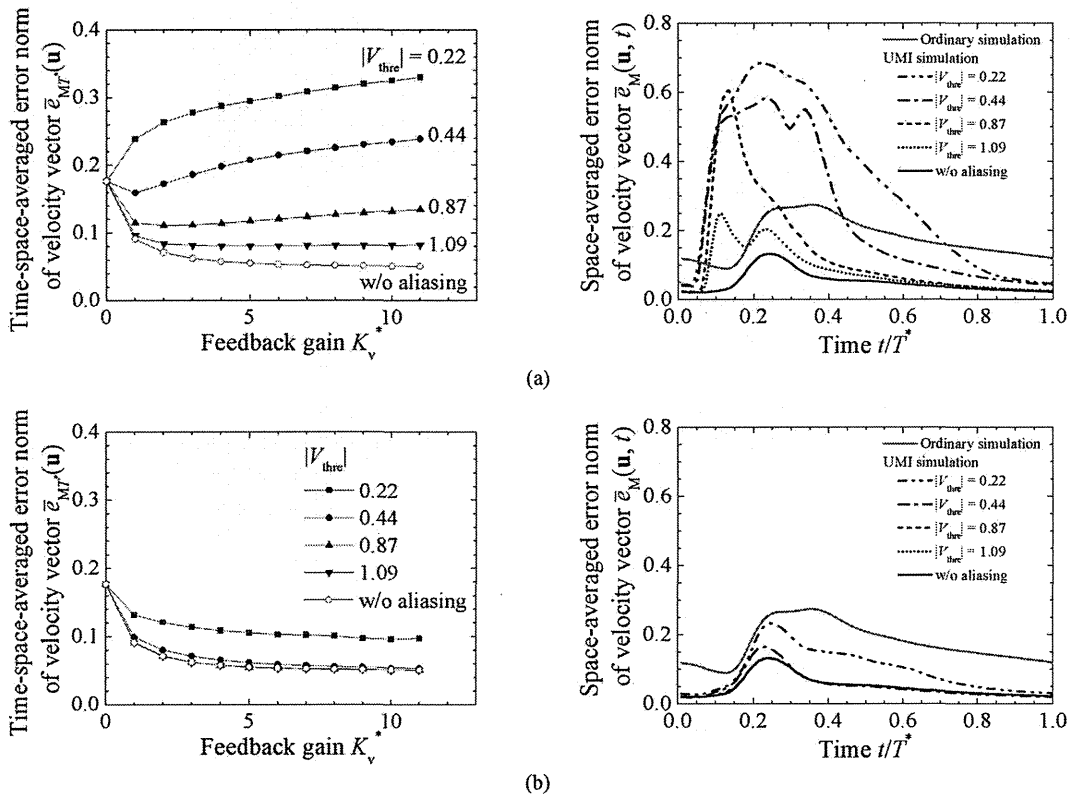

Fig. 8. Time-space-averaged (left column) and space-averaged error norms (right column) of the velocity vector of UMI simulations using aliased standard solution (a) without and (b) with a detection method for aliasing at $K_v^* = 11$.

same as that of the UMI simulation using the nonaliased standard solution except for the case of $|V_{\mathrm{thre}}| = 0.22$.

The contours of Doppler velocity on multiple cross sections of the aneurysm and the parent artery of the standard solution with aliasing ($|V_{\mathrm{thre}}| = 0.87$) at the timing of the maximum flow rate are represented in Fig. 9(a). Different from Fig. 7(a), displays with a reversal of colors are visible at locations where the Doppler velocity exceeds the threshold $|V_{\mathrm{thre}}|$: a region with cold color in the parent artery mainly on the leftmost vertical cross section (see a white arrow in Fig. 9(a)) and in a region with warm color at the neck of the aneurysm on the lowest horizontal cross section (see a black arrow). Using the standard solution with aliasing in the UMI simulation, feedback signals work in incorrect directions at the aliased points, resulting in a dark display, as shown in Fig. 9(b). In contrast, as shown in Fig. 9(c), a color Doppler image of the UMI simulation with the treatment for aliasing well reproduces the standard solution without measurement error of Fig. 7(a).

C. *Effect of Wall Filter*

In this subsection, the effect of wall filter, which forces small Doppler velocity to zero in the ultrasonic measurement, is evaluated.

Fig. 10(a) represents the relationship between the time-space-averaged error norm of velocity vector, $\bar{e}_{MT^*}(\mathbf{u})$, and the feedback gain, K_v^*, of the UMI simulations using the standard solutions in which small Doppler velocities are zeroed with wall filters ($|V_{\mathrm{WF}}| = 0.022$ or 0.087). Similar to the effect by Gaussian noise (see Fig. 5), the value of $\bar{e}_{MT^*}(\mathbf{u})$ increases with K_v^* in UMI simulation with the feedback of the standard solution

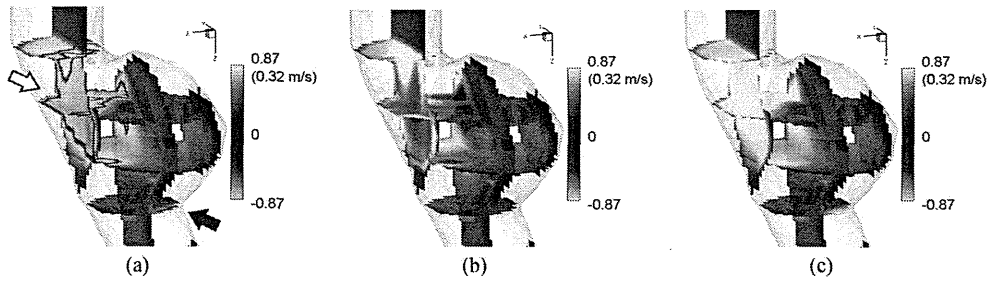

Fig. 9. Contour maps of Doppler velocity on four horizontal and three vertical planes at peak flow ($t/T^* = 0.13$): (a) the standard solution with aliasing with $|V_{\rm thre}| = 0.87$ (32 cm/s in dimensional value) and UMI simulations using the data "(a)" for feedback (b) without and (c) with detection method for aliasing at $K_{\rm v}^* = 11$. Black and white arrows indicate aliased regions.

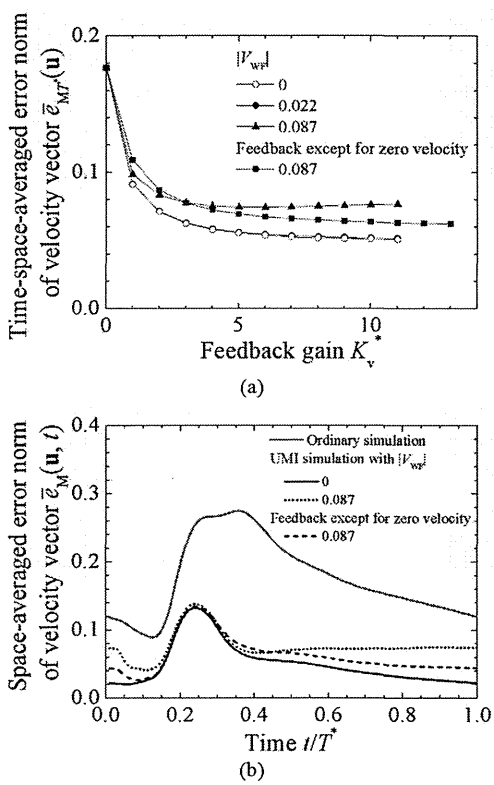

Fig. 10. (a) Variation of time-space-averaged error norm of velocity vector with feedback gain and (b) space-averaged error norm of velocity vector of UMI simulations with different degrees of wall filter, $|V_{\rm WF}|$, for feedback.

being processed by a wall filter with a relatively large value of $|V_{\rm WF}| = 0.087$. In this study, the effect of a wall filter on the UMI simulation was negligible in $|V_{\rm WF}| \leq 0.044$. This means that Doppler velocities reset to zero are originally slow, so that they do not much affect the whole flow field through the feedback process.

The computational accuracy of the UMI simulation ($K_{\rm v}^* = 11$) using the standard solution with the wall filter with $|V_{\rm WF}| = 0.087$ is evaluated at each time moment by the space-averaged error norm of the velocity vector, $\bar{e}_{\rm M}(\mathbf{u}, t)$ (see a dotted line in Fig. 10(b)). Enlargement of the error norm from the UMI simulation using the standard solution without the wall filter (black line) is observed, especially in diastole. This is because the information of Doppler velocity of the standard solution at many feedback points tends to be lost in diastole, being reset to zero (see Fig. 4(b)).

To prevent the feedback of filtered zero Doppler velocity in the UMI simulation, application of feedback signals was skipped at feedback points whose Doppler velocities of standard solution processed by a wall filter were zero. In Fig. 10, the error norms of the UMI simulation with treatment are also shown. With the treatment, the maximum value of feedback gain, with which numerical solution can be obtained without divergence, increases up to $K_{\rm v}^* = 13$ in the UMI simulation using the standard solution with the wall filter with $|V_{\rm WF}| = 0.087$ (see Fig. 10(a)). The value of $\bar{e}_{MT}(\mathbf{u})$ is repressed so as not to increase with the feedback gain by the treatment for the wall filter, though it is larger than that without the treatment in the range of small feedback gain. In the space-averaged error norm of the velocity vector in Fig. 10(b), a decrease of the error by the treatment is visible in diastole, showing a result equivalent to the UMI simulation using the standard solution without a wall filter ($|V_{\rm WF}| = 0$).

Contours of Doppler velocity of the standard solution on multiple cross sections in the aneurysm and the parent artery at $t/T^* = 0.61$ (0.60 s, dimensionally) in diastole are shown in Fig. 11(a). Applying the wall filter with $|V_{\rm WF}| = 0.087$ to the standard solution, the velocity adjacent to the blood vessel wall becomes zero, resulting in enlargement of the black region, as shown in Fig. 11(b). The UMI simulation (see Fig. 11(c)) using the data of Fig. 11(b), but not applying the feedback signals at feedback points whose Doppler velocities are zero, is similar to the standard solution without measurement errors of Fig. 11(a) for the sake of feedback. In contrast, the ordinary simulation without the feedback provides different patterns of contours as shown in Fig. 11(d).

Actually, more complicated MTI filters developed by various manufacturers are installed in ultrasonic measurement equipment to visualize only blood flow in color Doppler imaging. However, the basic concept of such filters is to regard regions with small velocity as tissue, ignoring the slow velocities. Therefore, though the above investigation with regard to the wall filter, by which all slow velocities less than a threshold value were changed to zero, may not be complete, it gives us fundamental insights for repressing the effect of MTI filters on the UMI simulation.

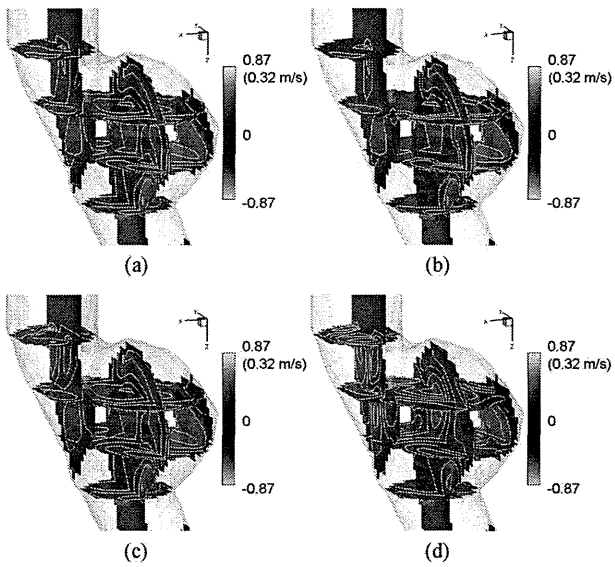

Fig. 11. Contour maps of Doppler velocity on four horizontal and three vertical planes in diastole ($t/T^* = 0.61$): standard solution (a) without and (b) with wall filter with $|V_{WF}| = 0.087$ (3.2 cm/s in dimensional value), (c) UMI simulation using the data "(b)" for feedback except for zero velocity at $K_v^* = 11$, and (d) ordinary simulation ($K_v^* = 0$).

D. *Effect of Lack of Data*

The time-space-averaged and space-averaged error norms of the velocity vector of the UMI simulation using the standard solution, whose Doppler velocities are randomly zeroed, are shown in Fig. 12. The error norms become large as the degree of the lack of data increases (see Fig. 12(a)). Especially in the cases with much lack of data ($N_{LD}/N_{FB} \geq 10\%$), error sharply decreases and then gradually increases with the feedback gain. Additionally, there are timings when the computational accuracy of the UMI simulation becomes worse than the ordinary simulation (see Fig. 12(b)).

Lack of data and wall filter are similar in terms of incorrect output of measured Doppler velocities as zero. Average percentages of feedback points whose Doppler velocities were processed by wall filters with $|V_{WF}| = 0.011, 0.022, 0.044$, and 0.087 in one cardiac cycle were $N_{WF}/N_{FB} = 6.9\%$, 13.5%, 25.5%, and 45.2%, respectively (see Fig. 4). Comparison of the space-averaged error norms of Doppler velocity between UMI simulations using the standard solution with those having almost the same percentages of N_{WF}/N_{FB} by a wall filter and N_{LD}/N_{FB} by a lack of data (see Figs. 10(b) and 12(b)), showed that error derived from the lack of data was more significant in the whole period. Accordingly, lack of measurement data has a greater influence on the UMI simulation than the wall filter since the fast Doppler velocity is reset as zero.

The same investigation as that for treatment of the wall filter was carried out for the lack of data; feedback was not applied at the feedback points whose Doppler velocities were zero. In Fig. 12, time-space-averaged and space-averaged error norms of the velocity vector of the UMI simulation with treatment for the lack of data ($N_{LD}/N_{FB} = 20\%$) are also shown. Only in the case of a lack of 20% of the data, a numerical solution without

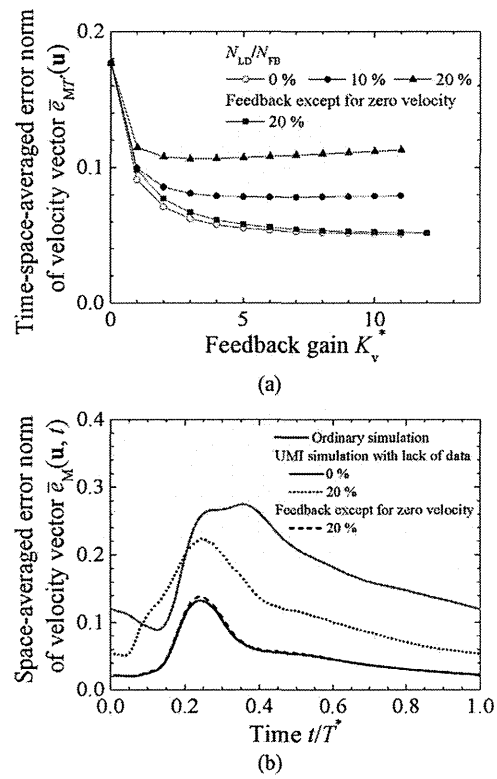

Fig. 12. (a) Variation of time-space-averaged error norm of velocity vector with feedback gain and (b) space-averaged error norm of velocity vector of UMI simulations with different degrees of lack of data for feedback.

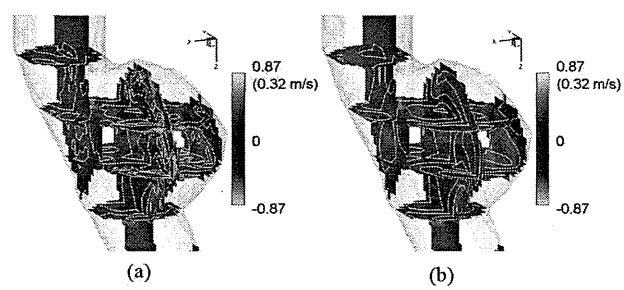

Fig. 13. Contour maps of Doppler velocity on four horizontal and three vertical planes in diastole ($t/T^* = 0.61$): (a) standard solution with lack of 20% of data, and (b) UMI simulation using the data "(a)" for feedback except for zero velocity at $K_v^* = 11$.

divergence is obtained even with the feedback gain of $K_v^* = 12$ in the UMI simulation. Owing to the treatment for a lack of data, the UMI simulation becomes able to provide almost the same result as that using the standard solution without measurement errors.

The result of Doppler velocities of the standard solution with a lack of 20% of the data at the same timing ($t/T^* = 0.61$) in Fig. 11 is visualized in Fig. 13(a). Since the Doppler velocities are randomly zeroed, the contour has many black dots, being different from Fig. 11(a). On the other hand, in Fig. 13(b), the UMI simulation using the standard solution of Fig. 13(a) but not applying the feedback at feedback points whose Doppler velocities are zero well reproduces the standard solution without lack of data of Fig. 11(a).

In ultrasonic measurement, there are two cases by which Doppler velocity becomes zero: blood flow velocity is actually zero, and the velocity is affected by measurement errors. Although it is difficult to distinguish them, it is possible to make the computational result approach the true blood flow field and to improve the computational accuracy by not applying feedback signals in cases in which the measured Doppler velocities are zero in the UMI simulation.

In the above discussion, effects of four measurement errors were investigated independently. But in a real situation, these errors appear simultaneously, and Gaussian noise may lead Doppler velocity to aliasing or zero velocity by increasing or decreasing the velocity magnitude. A combination of the present treatments is probably a solution in such a case, but it remains as a future work. In addition, scanning sequence and time in ultrasonic measurement were neglected. In order to more realistically mimic ultrasonic Doppler measurement, a sophisticated way has been proposed by Swillens *et al.* [21], [22], including the dynamics of scan sequencing and the statistics of velocity estimation process in ultrasound color Doppler imaging. In contrast, this study aimed at clarifying how each error in ultrasonic measurement influenced the blood flow field, especially in the 3-D velocity vectors, obtained by UMI simulation in detail. The results indicate the possibility that UMI simulation with treatments for aliasing and zero Doppler velocity at an appropriate feedback gain ($K_v^* < 12$) reproduces the blood flow field.

IV. Conclusion

Among measurement errors included in ultrasound Doppler measurement, effects of four major measurement errors, namely, those due to Gaussian noise, aliasing, wall filter, and lack of data, on UMI simulation were examined by a numerical experiment dealing with the same objective of blood flow field in the descending aorta with an aneurysm as that in our previous study. While solving the governing equations in a UMI simulation, Gaussian noise did not prevent the UMI simulation from effectively reproducing the blood flow field. In contrast, aliasing caused significant errors in the UMI simulation. Effects of wall filter and lack of data appeared in diastole and in the whole period, respectively. By detecting significantly large feedback signals as a sign of aliasing and by not adding feedback signals where measured Doppler velocities were aliasing or zero, the computational accuracy substantially improved, alleviating the effects of measurement errors. Based on these considerations, UMI simulation can be performed with suppression of four major measurement errors, and accurately provides detailed information on hemodynamics.

Acknowledgment

All computations were performed using the supercomputer system (SGI Altix 3700 B×2, SGI Japan, Tokyo, Japan) at the Advanced Fluid Information (AFI) Research Center, Institute of Fluid Science, Tohoku University.

References

[1] N. Depaola, M. A. Gimbrone, P. F. Davies, and C. F. Dewey, "Vascular endothelium responds to fluid shear-stress gradients," *Arterioscler. Thrombosis*, vol. 12, pp. 1254–1257, Nov. 1992.

[2] M. J. Levesque and R. M. Nerem, "The elongation and orientation of cultured endothelial-cells in response to shear-stress," *J. Biomech. Eng. Trans. ASME*, vol. 107, pp. 341–347, 1985.

[3] E. Sho, M. Sho, K. Hoshina, H. Kimura, T. K. Nakahashi, and R. L. Dalman, "Hemodynamic forces regulate mural macrophage infiltration in experimental aortic aneurysms," *Exp. Mol. Pathol.*, vol. 76, pp. 108–116, Apr. 2004.

[4] J. Suo, D. E. Ferrara, D. Sorescu, R. E. Guldberg, W. R. Taylor, and D. P. Giddens, "Hemodynamic shear stresses in mouse aortas—Implications for atherogenesis," *Arterioscler. Thrombosis Vascular Biol.*, vol. 27, pp. 346–351, Feb. 2007.

[5] D. A. Steinman, "Image-based computational fluid dynamics modeling in realistic arterial geometries," *Ann. Biomed. Eng.*, vol. 30, pp. 483–497, Apr. 2002.

[6] T. Hassan, E. V. Timofeev, T. Saito, H. Shimizu, M. Ezura, T. Tominaga, A. Takahashi, and K. Takayama, "Computational replicas: Anatomic reconstructions of cerebral vessels as volume numerical grids at three-dimensional angiography," *Amer. J. Neuroradiol.*, vol. 25, pp. 1356–1365, Sep. 2004.

[7] M. Shojima, M. Oshima, K. Takagi, R. Torii, M. Hayakawa, K. Katada, A. Morita, and T. Kirino, "Magnitude and role of wall shear stress on cerebral aneurysm—Computational fluid dynamic study of 20 middle cerebral artery aneurysms," *Stroke*, vol. 35, pp. 2500–2505, Nov. 2004.

[8] C. K. Zarins, D. P. Giddens, B. K. Bharadvaj, V. S. Sottiurai, R. F. Mabon, and S. Glagov, "Carotid Bifurcation atherosclerosis quantitative correlation of plaque localization with flow velocity profiles and wall shear-stress," *Circ. Res.*, vol. 53, pp. 502–514, 1983.

[9] E. S. Di Martino, G. Guadagni, A. Fumero, G. Ballerini, R. Spirito, P. Biglioli, and A. Redaelli, "Fluid–structure interaction within realistic three-dimensional models of the aneurysmatic aorta as a guidance to assess the risk of rupture of the aneurysm," *Med. Eng. Phys.*, vol. 23, pp. 647–655, Nov. 2001.

[10] K. R. Moyle, L. Antiga, and D. A. Steinman, "Inlet conditions for image-based CFD models of the carotid bifurcation: Is it reasonable to assume fully developed flow?" *J. Biomech. Eng. Trans. ASME*, vol. 128, pp. 371–379, Jun. 2006.

[11] T. Hayase and S. Hayashi, "State estimator of flow as an integrated computational method with the feedback of online experimental measurement," *J. Fluids Eng. Trans. ASME*, vol. 119, pp. 814–822, Dec. 1997.

[12] K. Nisugi, T. Hayase, and A. Shirai, "Fundamental study of hybrid wind tunnel integrating numerical simulation and experiment in analysis of flow field," *JSME Int. J. Ser. B Fluids Therm. Eng.*, vol. 47, pp. 593–604, Aug. 2004.

[13] T. Yamagata, T. Hayase, and H. Higuchi, "Effect of feedback data rate in PIV measurement-integrated simulation," *J. Fluid Sci. Technol.*, vol. 3, pp. 477–487, 2008.

[14] M. Nakao, K. Kawashima, and T. Kagawa, "Application of MI simulation using a turbulent model for unsteady orifice flow," *J. Fluids Eng. Trans. ASME*, vol. 131, pp. 111401-1–6, Nov. 2009.

[15] K. Funamoto, T. Hayase, Y. Saijo, and T. Yambe, "Numerical experiment of transient and steady characteristics of ultrasonic-measurement-integrated simulation in three-dimensional blood flow analysis," *Ann. Biomed. Eng.*, vol. 37, pp. 34–49, Jan. 2009.

[16] K. Funamoto, T. Hayase, Y. Saijo, and T. Yambe, "Numerical experiment for ultrasonic-measurement-integrated simulation of three-dimensional unsteady blood flow," *Ann. Biomed. Eng.*, vol. 36, pp. 1383–1397, Aug. 2008.

[17] K. Funamoto, Y. Suzuki, T. Hayase, T. Kosugi, and H. Isoda, "Numerical validation of MR-measurement-integrated simulation of blood flow in a cerebral aneurysm," *Ann. Biomed. Eng.*, vol. 37, pp. 1105–1116, Jun. 2009.

[18] K. Funamoto, T. Hayase, A. Shirai, Y. Saijo, and T. Yambe, "Fundamental study of ultrasonic-measurement-integrated simulation of real blood flow in the aorta," *Ann. Biomed. Eng.*, vol. 33, pp. 415–428, Apr. 2005.

[19] M. S. Olufsen, C. S. Peskin, W. Y. Kim, E. M. Pedersen, A. Nadim, and J. Larsen, "Numerical simulation and experimental validation of blood flow in arteries with structured-tree outflow conditions," *Ann. Biomed. Eng.*, vol. 28, pp. 1281–1299, Nov./Dec. 2000.

[20] K. Funamoto, T. Hayase, Y. Saijo, and T. Yambe, "Detection and correction of aliasing in ultrasonic measurement of blood flows with ultrasonic-measurement-integrated simulation," *Technol. Health Care*, vol. 13, pp. 331–344, Jul. 2005.
[21] A. Swillens, T. De Schryver, L. Lovstakken, H. Torp, and P. Segers, "Assessment of numerical simulation strategies for ultrasonic color blood flow imaging, based on a computer and experimental model of the carotid artery," *Ann. Biomed. Eng.*, vol. 37, pp. 2188–2199, Nov 2009.
[22] A. Swillens, L. Lovstakken, J. Kips, H. Torp, and P. Segers, "Ultrasound simulation of complex flow velocity fields based on computational fluid dynamics," *IEEE Trans. Ultrason. Ferroelectr. Freq. Control*, vol. 56, pp. 546–556, Mar. 2009.

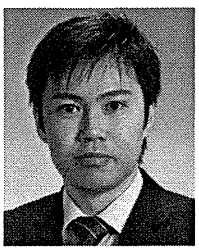

Kenichi Funamoto was born in Yamaguchi Prefecture, Japan, in 1979. He received the Ph.D. degree in engineering from Tohoku University, Sendai, Japan, in 2007.

Since 2008, he has been an Assistant Professor in the Institute of Fluid Science, Tohoku University. His current research interests include measurement-integrated simulation and blood flow analysis.

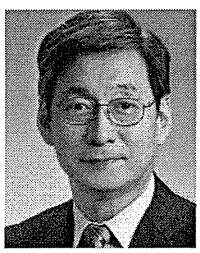

Toshiyuki Hayase was born in Nagoya, Japan, in 1956. He received the Ph.D. degree in engineering in 1987 from Nagoya University, Nagoya, Japan.

From 1980 to 1990, he was a Research Associate at Nagoya University. He became an Associate Professor of the Institute of Fluid Science, Tohoku University, Sendai, Japan, in 1990, and has been a Professor since 2000. His current research interests include the measurement-integrated simulation of complex flow problems.

Yoshifumi Saijo received the M.D. and Ph.D. degrees from Tohoku University, Sendai, Japan, in 1988 and 1993, respectively.

He is currently a Professor at the Graduate School of Biomedical Engineering, Tohoku University. His current research interests include high-resolution biomedical imaging with high-frequency ultrasound, blood flow analysis in the cardiovascular system, and parametric imaging with intravascular ultrasound or transesophageal echocardiography.

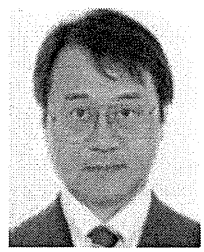

Tomoyuki Yambe received the Ph.D. degree in medicine from Tohoku University, Sendai, Japan, in 1989.

Since 2004, he has been a Professor in the Institute of Development, Aging and Cancer, Tohoku University. His current research interests include cardiology, artificial organs such as an artificial heart including totally implantable ventricular assist system, clinical application of ventricular assist devices, and an autonomic nervous system.

33rd Annual International Conference of the IEEE EMBS
Boston, Massachusetts USA, August 30 - September 3, 2011

Palpation Nonlinear Reaction Force Analysis for Characterization of Breast Tissues

Yo Kobayashi, *Member, IEEE,* Mariko Tsukune, Takeharu Hoshi, Tomoyuki Miyashita, Yasuyuki Shiraishi, Tomoyuki Yambe and Masakatsu G. Fujie, *Member, IEEE*

Abstract— **This paper addresses a diagnostic palpation system based on the measurement of nonlinear elasticity. An indentation probe is used to press against breast tissue. Then, the measured reaction force is used to estimate the parameters of nonlinear elasticity, which enables the identification of tissue type, such as fat, muscle, mammary gland or tumor. Here, we present the basic concept of our study and preliminary experimental and simulation results from pilot studies. More specifically, we measured the nonlinear response of reaction force using the breast of a goat. In addition, we also simulated the reaction force using nonlinear biomechanical simulation with several tissue types. Large differences in reaction force occur only in the nonlinear range in both experimental and simulation situations. Our results confirmed the feasibility of our concept.**

I. Introduction

BREST cancer accounts for more than 1 million of the estimated 10 million malignancies diagnosed worldwide each year. In recent years, early detection of breast cancer has been possible because of advances in imaging technology. However, it is difficult to locate the exact position of a tumor and to make a definite diagnosis by palpation or imaging. In addition, invasive examinations such as biopsy are needed to diagnose whether a breast tumor is benign or malignant. Non-invasive and accurate diagnostic techniques are, therefore, desired to achieve accurate diagnosis and to alleviate the patient's mental burden.

The stiffness of malignant tumors has traditionally been qualitatively measured based on palpation by doctors. Many studies have reported systems for tissue characterization and for locating exact tumor position based on palpation. In particular, elastography imaging technologies have been explored. Elastography requires the induction of motion within the target tissue by an external force and conventional medical imaging modalities are used to measure tissue deformation, from which mechanical properties can be reconstructed.

There are limitations in the present elastography protocols. Elastography imaging typically provides contrast in linear stiffness under the assumption of very small deformations. It is actually very difficult to measure nonlinear properties using large deformations. On the other hand, tissues generally exhibit homogeneous, nonlinear, anisotropic elastic and viscous behaviors [1]. Krouskop et al. [2], Wellman et al. [3] and Samani et al. [4] measured the stiffness properties of breast tissues. These papers reported that breast tissue exhibits strong nonlinear properties. More specifically, tissues under low stress exhibit linear properties, but stiffness increased in tissues under high stress. The authors have also reported the measurement of nonlinear elastic properties of breast soft tissues, such as fatty tissue, muscles and mammary glands [5]. They reported that there are large differences in the magnitude of nonlinear elasticity among breast tissues, while differences in elastic properties in the linear range are small.

The goal of this study is to develop a diagnostic palpation system to identify the location of each tissue based on the measurement of nonlinear elasticity. Figure 1 shows our system concept. The indentation probe presses against breast tissue to the extent that the strains of breast tissue become large and such that nonlinear properties are exhibited. Then, the measured reaction force is used to estimate the parameters of nonlinear elasticity. The type of tissue, such as fat, muscle, mammary grand or tumor is identified by the estimated parameters of nonlinear elasticity. In addition, we consider that nonlinear elasticity measurement can be an effective method for the identification of tumor type because Krouskop et al. [2] have shown that nonlinear elasticity of malignant tumor is larger than that of benign tumor.

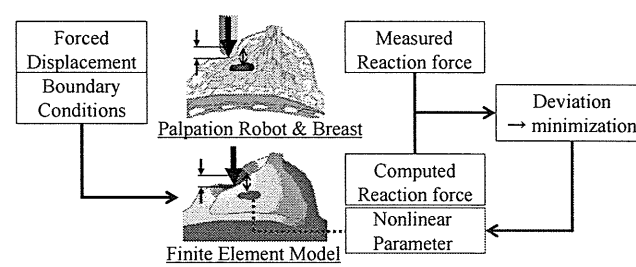

Fig.1. The conceptual scheme of our palpation method.

Manuscript received April 15th, 2011. This work was supported, in part, by the Global COE Program "Global Robot Academia" from MEXT (Ministry of Education, Culture, Sports, Science and Technology of Japan), a High-Tech Research Center Project from MEXT, a Grant-in-Aid for Scientific Research from MEXT (no. 22360108 and 22103512), a Waseda University Grant for Special Research Projects (no. 2010B-177) and Cooperative Research Project of the Institute of Development, Aging and Cancer, Tohoku University.

Y. Kobayashi is with the Faculty of Science and Engineering, Waseda University, Japan. (59-309, 3-4-1 Ohkubo Shinjuku-ku, Tokyo, Japan, phone: +81-3-5286-3412; fax: +81-3-5291-8269; e-mail: you-k@fuji.waseda.jp).

M. Tsukune is with the Graduate School of Science and Engineering, Waseda University, Japan.

T. Hoshi, T. Miyashita and M. G. Fujie are with the Faculty of Science and Engineering, Waseda University, Japan.

Y. Shiraishi and T. Yambe are with the Department of Medical Engineering and Cardiology, Institute of Development, Aging and Cancer, Tohoku University

It should be noted that there are some studies in the field of elastography addressing nonlinear elasticity. For example, Hall et al. present a system for nonlinearity imaging by 1% incremental strain [6]. Nitta et al. have described nonlinear elasticity parameter estimations for kidney phantom [7]. Wang et al. present an elastography method for reconstruction of nonlinear breast tissue properties and for simulation investigation [8]. These papers propose methods to identify nonlinear parameters but experimental evaluation with actual animal tissues were not conducted [7] [8]. Hall et al. [6] reported experiments and evaluation with actual tissue, although the experiment was conducted with only small displacements. In short, tissue characterization using analysis of nonlinear reaction force with large deformation has not been conducted.

The objective of the present paper is to investigate the basic concept of our study using preliminary experimental and simulation studies. More specifically, we used goat breast to measure the reaction force in response to large deformation. In addition, we also simulated the reaction force using nonlinear biomechanical simulation in several tissue types. The feasibility of our concept, tissue identification based on nonlinear properties of tissues, is discussed.

II. METHOD

A. Experiment

In this section, we describe the conditions under which the in vivo experiment was conducted. The method was performed using a test apparatus implanted in the breast of a goat. We intended to measure the reaction force from two indentation points in which the ratio of tissues (fats and mammary gland) are different under each point. The experimental details are described below (Fig. 2).

1) Ethical issues: All animals received humane care in accordance with "The Guidelines for the Care and Use of Laboratory Animals" published by the National Institute of Health (NIH publication 85-23, revised 1985), "The Guidelines for Proper Conduct of Animal Experiments" formulated by the Science Council of Japan (2006), and the guidelines determined by the Institutional Animal Care and Use Committee of Tohoku University.

2) Experimental setup: A goat breast was used for in vivo experiments. The goat was placed supine as shown in Fig. 2. In humans, the sternum is located under the breast, which acts as a stiff boundary (refer to Fig. 3). Unlike humans, goats have no sternum under their breast. As a boundary condition, considering the effect of the sternum in humans, we set the dorsal area of the goat breast as the fixed boundary by inserting a metal plate as shown in Fig. 3.

3) Experimental apparatus: The experimental manipulator has one degree of freedom of linear movement by an actuator. A force sensor (NANO 1.2/1, BL AUTOTEC) and a 7 mm diameter indentation probe were attached to the manipulator as shown in Fig. 2. We calculated the moving distance of the probe from the value of the encoder attached to the motor. The reactive forces exerted on the probe were sampled by the force sensor.

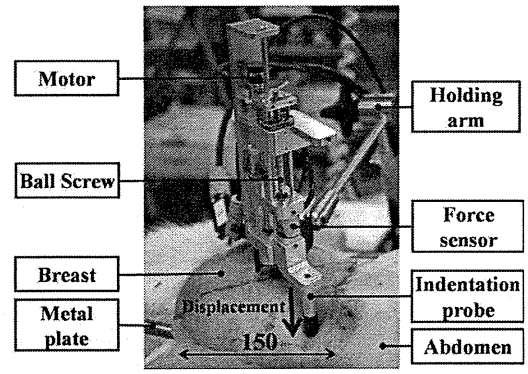

Fig.2. The arrangement of the goat breast and apparatus.

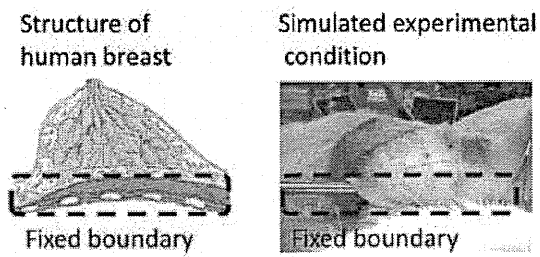

Fig.3. The boundary conditions of the breast in vivo.

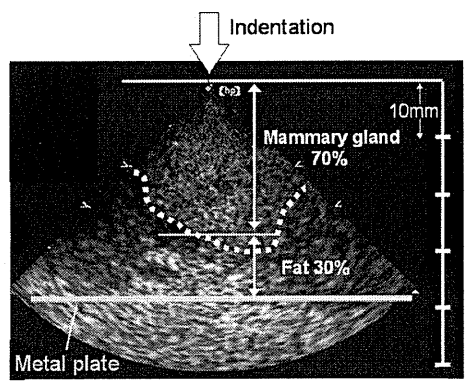

(a) Point A

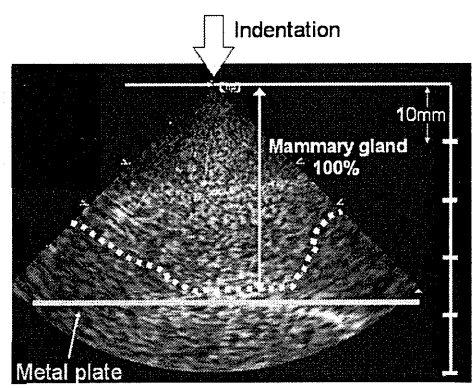

(b) Point B

Fig.4. Ultrasound images of hog breast at each point

4) Imaging modality: Ultrasound equipment (SONOS 5500, Hewlett Packard) was used for imaging because of its compatibility with the robot and for its ability to show real-time visualization.

5) Experimental conditions and procedures: First, we searched for an indentation point using an ultrasound probe. We judged the ratio of fats to mammary gland under the search point from the contrast of ultrasound images. We determined two points in which the ratio of fat and mammary grand are different: under point A, the tissue ratio was 70% mammary gland to 30% fat and at point B the tissue ratio was 100% mammary gland to 0% fat. The ultrasound images at each point are shown in Fig.4. For each point we positioned the experimental apparatus and fixed it in place using a laparoscope positioning device that can be changed between a free state and a locked state. The indentation was then carried out at constant velocity 3.0 mm/s and the force and displacement of the probe were recorded. Three indentations were performed at each point. We performed the experiment at point A and B.

B. Simulation

We have developed and reported mechanical liver and breast models in previous papers, in which we also gave specific descriptions of the material properties of the liver and of finite element based modeling (FEM) and of FEM validation [9]-[10]. The nonlinear force analysis was carried out using this modeling method. An overview of this modeling is presented as follows:

1) Material nonlinearity: We have previously reported the nonlinear elastic model of a pig liver [9] and breast [5]. This model was constructed by the torsional creep test using a rheometer (AR-G2, TA-Instrument). A creep test was carried out for various stresses to investigate material nonlinear properties. In our previous work, the steady state of the step response following sufficient elapsed time exhibits the low-frequency characteristics described in (1). Nonlinear properties can be modeled using the quadric function of strain described in equation (2). The parameters of these equations, measured by the experiment, are shown in Table I.

$$G\frac{d^k\gamma}{dt^k}=\tau \tag{1}$$

$$G=\begin{cases} G_o & (\gamma<\gamma_0) \\ G_0(1+a(\gamma-\gamma_0)^2) & (\gamma>\gamma_0) \end{cases} \tag{2}$$

where G is the magnitude of stiffness, G_o is the viscoelastic modulus of the linear range, a_γ is the coefficient when the change of γ is the shear strain and γ_0 is the strain in which the characteristics of soft tissue change show nonlinearity.

2) Finite element modeling: We have previously reported our solution for the finite element model and have also provided specific descriptions of the development of this model [9]-[10]. As shown in Fig. 5, a model was constructed with a breast shape similar to that of the breast used in the experiment, which is explained in section A. The shape of the breast model was assumed to be 40 mm square. As a boundary condition, we set the dorsal side of the model as the fixed end simulating the effect of the sternum (we used a metal plate in the experiment). The mesh was developed using the Delaunay method, which involves dividing the object automatically into triangular elements, based on the outline of the target object. This is one of the most accepted methods because of the uniquely high reliability resulting from its geometric division. We created the two models with the same shape and mesh but having different material properties: one consisted of 70% mammary gland and 30% fat; the other consisted of 100% mammary gland and 0% fat. The configuration of mesh and each tissue is presented in Fig. 5.

3) Material properties: The stiffness parameter of the model was decided based on our previous work to measure the nonlinear elasticity of breast tissues [5]. Our previous work [9] revealed that there are large differences between the stiffness parameters of in vitro tissue and in vivo tissue. Considering the above, linear elasticity G_o was manually set to correspond with the experimental results shown in Fig.6. Meanwhile, the nonlinear elastic parameters a_γ and γ_0 were not changed for the evaluation by difference in nonlinear elasticity. Table I shows the parameters of each tissue.

4) Simulation conditions: Nodes at probe contact at the center of the upper surface were displaced along the Y-axis at a rate of 3.0 mm/s. Time-series data for probe displacement and the external force were collected during the simulation. The simulations were carried out for both models.

III. Results

Figure 6 presents the experimental results of the reaction force during the indentations. Both reaction forces at point A and B increased linearly in response to small displacements of the indentation probe. The slopes of force increase were at similar magnitudes. The reaction force at point B exhibits a nonlinear increase after 4 mm of probe displacement. Meanwhile the force at point A remained linear after approximately 8 mm of displacement.

Figure 6 also presents the simulation results of the reaction force. The tendency was the same as in the experimental results; a small difference in reaction force in the linear range in response to small displacement and a large difference in the reaction force in the nonlinear range in response to large

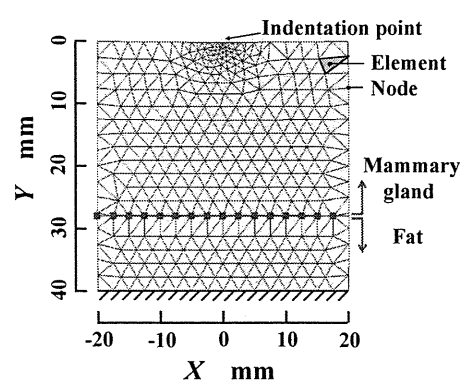

Fig.5. Boundary conditions of breast model mesh. The rear side of the model was set to be the fixed end.

TABLE I
PARAMETER OF EACH TISSUE OF THE BREAST MODEL

Tissue type	G_0 Pa	γ_0	a_γ
Fat	3.0×10^3	0.87	2.1
Mammary gland	4.8×10^3	0.44	2.1×10^1

displacement. The reaction force in the simulation was small in both nonlinear and linear ranges compared with the experimental result. The magnitude of nonlinearity in the simulation was also small compared with the experimental results.

IV. Discussion

1) Feasibility of our concept: There were small differences in the linear range in the reaction force during small displacements between the experimental and simulation results. On the other hand, this difference became large when the probe displacement became large and the reaction force became nonlinear. A small difference of reaction force may result in mischaracterization of tissue. Therefore, we suggest that it is preferable to identify tissue type by evaluating nonlinear elasticity rather than linear elasticity. These results support the feasibility of our concept to evaluate the nonlinear reaction force following large deformation of the breast.

2) Two dimensional analysis and model shape: we developed a 2D liver model and provided a 2D deformation simulation. It is acknowledged that a 3D model would provide more accurate results. However, an assumption, supported by related studies [11], was made that 2D simulation and manipulator movement would be sufficiently effective to enable accurate needle insertion. A comparative evaluation of 2D and 3D simulation will be undertaken in future work. The other limitation in our investigation is the shape of the model. We simulated the reaction force with a simplified structure.

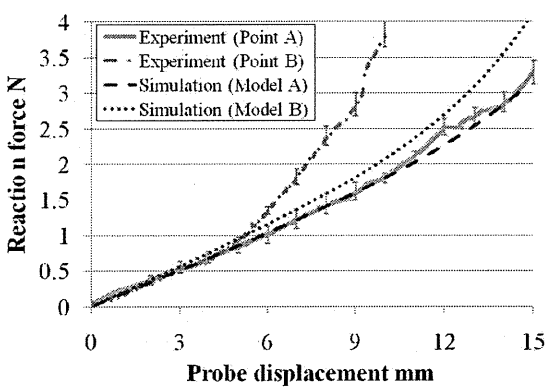

Fig.6. Experimental and simulation results of the reaction force (Average value of three experiments).

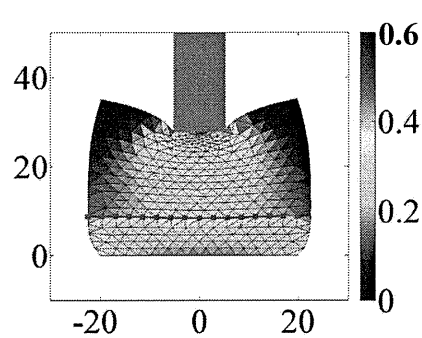

Fig.7. An example of model deformation. The color of each element represents the strain of the element.

The actual shape of the breast used in square breast model as the experiment was not square but a more complex structure. It is likely that the limitations of dimension and shape of the model result in the difference between the simulation and experimental results.

3) Tissue limitation: This article only covered mammary gland and fat as target tissues. The goal of our research is to characterize all the constituent breast tissues. Tissues such as muscle and tumor will be addressed in future work.

V. Summary And Future Work

We propose the palpation diagnosis system based on the measurement of nonlinear elasticity to identify the location of each breast tissue. Here, we have presented the basic concept of our study with preliminary experiment and simulation. More specifically, we performed an experiment to measure the nonlinear response of reaction force using the breast of a goat. In addition, we also simulated the reaction force using a nonlinear biomechanical simulation with several tissue types. Large differences in reaction force occur only in the nonlinear range in both experimental and simulation situations. Our results confirmed the feasibility of our concept.

In future work, we will examine the reaction force with a 3D breast model. We will perform an investigation that will include breast muscle and tumor. From these results, we will develop a palpation system for tissue characterization.

References

[1] N. Famaey, J. V. Sloten, "Soft tissue modelling for applications in virtual surgery and surgical robotics", *J. Comp. Meth. Biomech. and Bio-med. Eng.*, vol. 11, no. 4, pp. 351-366, 2008.

[2] T. A. Krouskop, T. M. Wheeler, F. Kallel, B. S. Garra, T. Hall, "Elastic moduli of breast and prostate tissues under compression", *Ultrason.. Imaging*, vol.20, pp. 260-274, 1998.

[3] P. S. Wellman, "Breast Tissue Stiffness in Compression is Correlated to Histological Diagnosis", PhD dissertation, Harvard University, USA, 1999.

[4] A Samani, "Measurement of the hyperelastic properties of 44 pathological ex vivo breast tissue samples", Institute of Physics and Engineering in Medicine, vol. 54, pp. 2557–2569, 2009

[5] M. Tsukune, .Y Kobayashi, T. Hoshi, T. Miyashita and M.G. Fujie, Member," Measuring the nonlinear elastic properties of soft tissues that compose breast and comparison of measurement results", in *33rd Annu. Int. Conf. IEEE EMBS*, accepted for publication, 2011.

[6] T. J. Hall, A. A. Oberai, P. E. Barbone, A. M. Sommer, N. H. Gokhale S. Goenezen and J. Jiang, "Elastic Nonlinearity Imaging", 31st Annual International Conference of the IEEE EMBS, pp. 1967-1970

[7] N. Nitta and T. Shiina, "Estimation of Nonlinear Elasticity Parameter of Tissues by Ultrasound", *Jpn. J. Appl. Phys.* vol. 41 pp. 3572–3578, 2002

[8] Z. G. Wang, Y. Liu, G. Wang, and L. Z. Sun, "Elastography Method for Reconstruction of Nonlinear Breast Tissue Properties", Int. J. Biomed. Imag., vol. 2009, Article ID 406854, 9 pages doi:10.1155/2009/406854

[9] Y. Kobayashi et al., " Development and validation of a viscoelastic and nonlinear liver model for needle insertion", International Journal of Computer Assisted Radiology and Surgery, Vol. 4(1), pp.53-63, 2009

[10] Y. Kobayashi et al., , "A Robotic Palpation-Based Needle Insertion Method for Diagnostic Biopsy and Treatment of Breast Cancer", in Proc. 2009 IEEE Int. Conf. Intelligent Robots and Systems, 2009, pp.5534-5539.

[11] S. P. DiMaio, and S. E. Salcudean "Needle insertion modeling and simulation," *IEEE Trans. Robot. Autom.*, vol. 19, no. 5, pp. 864–875, 2003.